*Molecular Physics*, 2015
Vol. 113, Nos. 3–4, 297–313, http://dx.doi.org/10.1080/00268976.2014.938709





## INVITED ARTICLE

# In honour of N. Yngve Öhrn: surveying proton cancer therapy reactions with Öhrn's electron nuclear dynamics method. Aqueous clusters radiolysis and DNA-base damage by proton collisions[1]

Patrick M. Mclaurin[a], Austin J. Privett[a], Christopher Stopera[a,2], Thomas V. Grimes[a], Ajith Perera[a,b] and Jorge A. Morales[a,*]

[a]*Department of Chemistry and Biochemistry, Texas Tech University, Lubbock, TX, USA;* [b]*Department of Chemistry, Quantum Theory Project, University of Florida, Gainesville, FL, USA*

(*Received 30 April 2014; accepted 15 June 2014*)

Proton cancer therapy (PCT) utilises high-energy $H^+$ projectiles to cure cancer. PCT healing arises from its DNA damage in cancerous cells, which is mostly inflicted by the products from PCT water radiolysis reactions. While clinically established, a complete microscopic understanding of PCT remains elusive. To help in the microscopic elucidation of PCT, Professor Öhrn's simplest-level electron nuclear dynamics (SLEND) method is herein applied to $H^+ + (H_2O)_{3-4}$ and $H^+ +$ DNA-bases at $E_{Lab} = 1.0$ keV. These are two types of computationally feasible prototypes to study water radiolysis reactions and $H^+$-induced DNA damage, respectively. SLEND is a time-dependent, variational, non-adiabatic and direct-dynamics method that adopts a nuclear classical-mechanics description and an electronic single-determinantal wavefunction. Additionally, our SLEND + effective-core-potential method is herein employed to simulate some computationally demanding PCT reactions. Due to these attributes, SLEND proves appropriate for the simulation of various types of PCT reactions accurately and feasibly. $H^+ + (H_2O)_{3-4}$ simulations reveal two main processes: $H^+$ projectile scattering and the simultaneous formation of H and OH fragments; the latter process is quantified through total integrals cross sections. $H^+ +$ DNA-base simulations reveal atoms and groups displacements, ring openings and base-to-proton electron transfers as predominant damage processes.

**Keywords:** electron nuclear dynamics; non-adiabatic dynamics; proton cancer therapy; water radiolysis; DNA-base damage

## 1. Introduction

Proton cancer therapy (PCT) employs high-energy $H^+$ projectiles to destroy cancerous cells [1–4]. The $H^+$ projectiles start in a collimated beam at an initial kinetic energy of 200–430 MeV, steadily lose their energy while penetrating the patient's body, and end up at a thermal energy when captured/combined in deep tissues. In all types of cancer radiation therapies (PCT, X-ray therapy, $^{12}C^{+6}$ therapy, etc.), the therapeutic effect ultimately results from the radiation damage on cellular DNA [1–4]. Having a high rate of division and reduced ability to repair damaged DNA, cancerous cells are much more susceptible to radiation-induced DNA damage than normal cells, and are killed at a much higher rate [1–4]. The greatest DNA damage occurs where maximum energy transfers from the radiation to the tissues. In a graph plotting the radiation dose vs. the radiation travelled distance, PCT exhibits a maximum – the so-called Bragg peak – very sharply just before the $H^+$ projectiles are stopped in the deep tissues. In contrast, conventional X-ray therapy exhibits a broader Bragg peak just after the photons' penetration into the body that is followed by a gradual dose decline. Thus, unlike X-ray therapy, PCT can produce maximum damage to a deep cancerous area with minimum damage to the surrounding healthy tissues.

In PCT, the $H^+$ projectiles predominantly collide with $H_2O$ molecules since these constitute ∼70% of the human cell mass. The $H^+$–$H_2O$ collisions give rise to various cascade reactions that produce (cf. Figure 1): (1) Free radicals (e.g. $H^+ + H_2O \rightarrow H^+ + H + OH$); (2) secondary ions (e.g. $H^+ + H_2O \rightarrow 2H^+ + OH^-$); (3) reactive molecules (e.g. $H^+ + 2H_2O \rightarrow H^+ + H_2 + H_2O_2$); (4) solvated/scattered electrons (e.g. $H^+ + H_2O \rightarrow H^+ +$

* Corresponding author. Email: jorge.morales@ttu.edu

[1] The authors warmly dedicate this SLEND investigation in honour of Professor N. Yngve Öhrn on the occasion of his 80th birthday celebration during the 54th Sanibel Symposium in St. Simons' Island, Georgia, on February 16–21, 2014. Associate Professor Jorge A. Morales was a former chemistry PhD student under the mentorship of Professor Öhrn and Dr Ajith Perera took various quantum chemistry courses taught by Professor Öhrn during his chemistry PhD studies. Both Jorge and Ajith look back to those great times of their scientific formation under Yngve's guidance during the 1990s with a strong sense of gratitude toward him (and even with a sense of nostalgia). The authors are pleased to present to Professor Öhrn this birthday gift of fully mature SLEND developments that now venture to treat systems of biochemical interest.

[2] Present address: Department of Chemistry and Industrial Hygiene, University of North Alabama, Florence, AL 35632-0001.

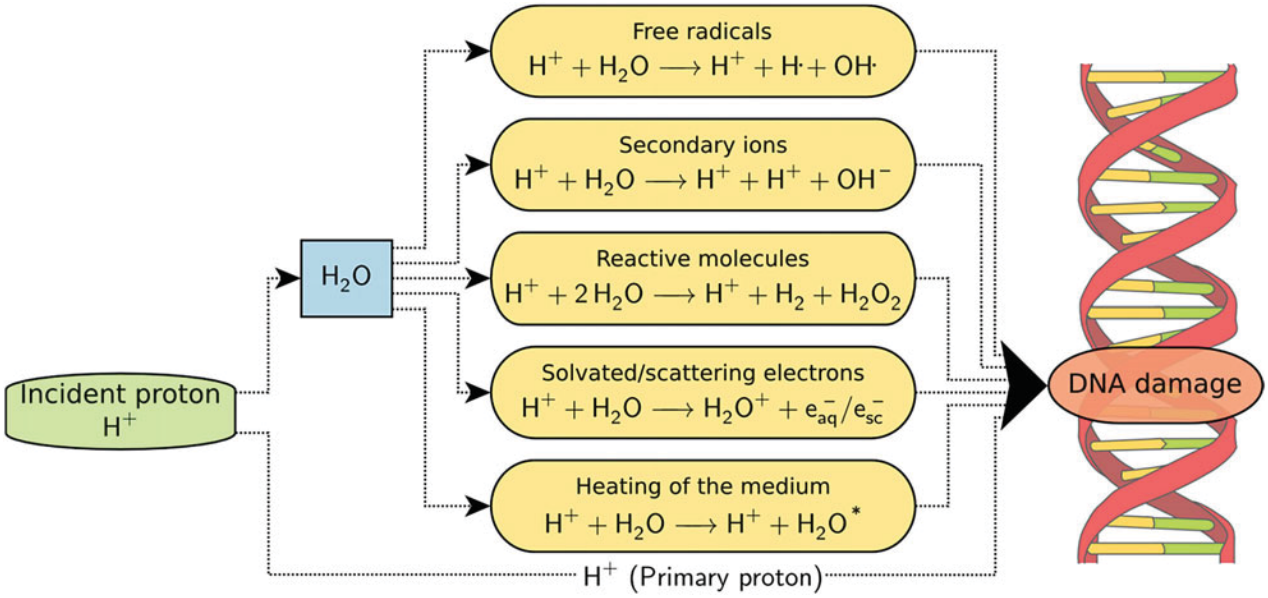


Figure 1. Flowchart of the main reactions and processes leading to DNA damage in PCT.

$H_2O + e^-_{(aq)/sc}$); and (5) heating of the medium [1,4,5]. The PCT reactions 1 through 4 are collectively known as water radiolysis reactions. The highly reactive products and heat from these reactions can eventually reach cellular DNA and cause various types of damage (e.g. DNA-bases' fragmentations and deletions, sugar–phosphate lesions and single- and double-strand breaks [1,4]). Additionally, to a lesser extent, primary $H^+$ projectiles can directly damage cellular DNA as well (cf. Figure 1).

While the clinical use of PCT as a substitute to X-ray therapy is definitely established, a complete understanding of the relationship between the above PCT reactions and their eventual effect on DNA damage and cancer cure remains elusive [1]. Various factors have precluded the attainment of that understanding within the traditional experimental-clinical paradigm in cancer research, but two main factors stand out: (1) The variety and complexity of the simultaneous PCT reactions, a situation defying any experimental technique, and (2) the possibility to put human subjects and/or patients at risk during tests. Accordingly, several theoretical/computational methods have been applied to the study and prediction of PCT reactions since those methods overcome the aforesaid complications in a virtual manner [1,4–10]. The PCT reactions and processes span different space ($l = 10^{-10} - 10^{-1}$ m) and time ($t = 10^{-21} - 10^{2}$ s) scales that determine the selection of an appropriate theoretical/computational method. Thus, reactions at the microscopic scale (roughly, $l \leq 10^{-9}$ m $= 10$ Å $= 18.9$ a.u. and $t \leq 10^{-13}$ s $= 100$ fs $= 4134$ a.u.) can be studied with quantum-mechanics methods at a reasonable computational cost. The aforesaid PCT water radiolysis reactions and the early DNA damage reactions initially localised on small DNA units belong to the microscopic scale; those reactions are, therefore, amenable to quantum-mechanics treatments. However, late DNA damage reactions over DNA molecules and tumour remission processes belong to the mesoscopic and macroscopic scales, respectively; those processes are only amenable to classical-mechanics Monte Carlo (CMMC) treatments [9–11]. Despite drastic differences in their theoretical framework, quantum-mechanics and CMMC methods act in synergy to solve PCT problems because prediction-level results from quantum-mechanics methods (e.g. reaction cross sections) constitute the necessary input data for CMMC simulations [5,9–11]; reciprocally, results from CMMC simulations reveal the mesoscopic and macroscopic manifestations of the microscopic processes underlying PCT [5,9–11]. As its title implies, this article will be exclusively concerned with the investigation of PCT reactions at the microscopic scale with quantum-mechanics methods.

In recent years, there has been a keen interest in studying different types of PCT reactions at the microscopic scale with various quantum-mechanics methods. In those studies, large PCT systems are customarily represented by smaller portions of themselves to obtain computationally feasible prototypes that display essential PCT processes. For instance, Pichl *et al.* [5] simulated $H^+ + H_2O$ collisions in the energy range $E_{Lab} = 50.0$–$1.0$ MeV using the electronic-state close-coupling method in conjunction with high-level pre-computed potential energy surfaces (PESs); this $H^+ + H_2O$ collision system constituted a tractable prototype to study actual PCT water radiolysis reactions in cellular bulk water (cf. Figure 1). In another study,

Champion *et al*. [8] investigated the collision systems: $H^+ + B$, B = adenine, cytosine, thymine and uracil, in the energy range $E_{Lab} = 1$–1000 keV with the continuum distorted wave (CDW) and CDW-eikonal initial state (CDW-EIS) approximations; these collision systems constituted tractable prototypes to study actual $H^+$ collisions with DNA/RNA bases bonded to cellular DNA/RNA (cf. Figure 1; for additional examples of quantum-mechanics studies of PCT reactions, the reader can consult the *Advances in Quantum Chemistry* Vol. 52 edited by J.R. Sabin and E.K. Brändas, which is entirely devoted to theoretical studies of the interaction of radiation with biomolecules).

The discussed theoretical studies have shed light onto important microscopic aspects of PCT, but a great deal of research remains to be conducted in order to attain a complete microscopic elucidation of PCT. A pressing need for that endeavor is to have a versatile method capable of simulating several types of PCT reactions both accurately and feasibly. Based on its long and successful research record, we believe that the electron nuclear dynamics (END) method at its simplest level (SL: SLEND) [12,13] qualifies for such a role. The END method created by E. Deumens and N.Y. Öhrn provides a time-dependent, variational, direct and non-adiabatic framework to simulate scattering processes and chemical reactions [12,13]. END admits several realisations according to the level of sophistication conferred to its trial wavefunction [12,13] (e.g. multi-configuration [14] or coupled-cluster [15] electronic wavefunctions or a Kohn–Sham density functional theory (KSDFT) formulation, as is the case of our own SLEND/KSDFT method [4,16]). SLEND adopts classical mechanics and a single-determinantal wavefunction for the nuclear and electronic degrees of freedom, respectively [12,13]. These features make SLEND computationally suitable for simulating large PCT systems. In addition, due to its direct-dynamics nature, SLEND (and any other END realisation) does not require pre-calculated PESs for its simulations since the potential energy and molecular forces among reactants are calculated 'on the fly' as a simulation proceeds. This is critical to efficiently treat large PCT-related systems (e.g. DNA bases and nucleotides), for which the construction of complete PESs becomes computationally impractical. Finally, what makes SLEND particularly suitable to study PCT reactions is its capacity to accurately describe the various simultaneous processes occurring during high-energy reactions. These processes include collision-induced rovibrational excitations, dissociation, substitution and rearrangements reactions, and non-adiabatic electron excitations and transfers [4]. It should be noticed that standard Born–Oppenheimer (adiabatic) direct dynamics methods solely implying the electronic ground state [17] cannot describe processes involving electronic excited states and exhibiting non-adiabatic electron excitations and transfers [4]. The versatility of SLEND to accurately describe those processes has been documented by its applications to numerous types of reactions at intermediate and high energies such as proton–molecule ($H^+ + H_2$ [18,19], $H^+ + CH_4$ [20], $H^+ + H_2O$ [21], $H^+ + C_2H_2$ [22,23], $H^+ + HF$ [24], $H^+ + CF_4$ [25], $H^+ + N_2$ [26], $H^+ + CO$ [27], and $H^+ + NO$ [28]), hydrogen–molecule ($H + D_2$ [29] and $H + HOD$ [30]), and molecule–molecule ($D_2 + NH_3$ [31], $S_N2$ [4] and Diels–Alder [4]) reactions, *inter alia* (for the latest theoretical developments and applications of SLEND, cf. our review chapter Ref. [4]).

Pioneering applications of SLEND to PCT reactions have been conducted by Cabrera-Trujillo *et al*. [6] and by Quinet *et al*. [7], who simulated the collision systems: $H^+ + H_2O$ and $H^+ + (H_2O)_2$, respectively, in the keV energy regime as tractable prototypes to study PCT water radiolysis reactions (cf. Figure 1). These two studies mostly concentrated on the qualitative description of collision-induced fragmentation reactions, although the second study provided preliminary integrals cross sections (ICSs) for some of those reactions [7]. Inspired by these previous studies, we decided to further extend the application of SLEND to PCT reactions and conducted the present SLEND investigation of the reactive systems: $H^+ + (H_2O)_{3-4}$ and $H^+ + B$, B = adenine, cytosine, guanine and thymine, all at $E_{Lab} = 1$ keV. These studies involving the aqueous clusters (ACs) $(H_2O)_{3-4}$ extend the trend in the previous studies involving the monomer $H_2O$ [6] and dimer $(H_2O)_2$ [7] ACs toward better prototypical descriptions of PCT water radiolysis reactions in cellular bulk water. In addition, the studied reactive systems involving the four possible DNA bases constitute tractable prototypes to study $H^+$ collisions with bases bonded to cellular DNA [here, the colliding $H^+$ projectiles represent either primary $H^+$ projectiles or secondary, tertiary, etc., $H^+$ projectiles produced by the PCT water radiolysis reactions (cf. Figure 1)]. The systems studied herein are among the largest ones simulated with SLEND to date [4]. While quantitative results are presented (e.g. reactions' ICSs), this investigation mostly provides a qualitative survey of the different types of collision-induced reactions occurring in the present PCT systems, as was also the case in the previous SLEND studies of $H^+ + (H_2O)_{1-2}$ [6,7]. This survey characterising all the possible reactive channels in the present systems is the necessary 'road map' to start more demanding studies aimed at predicting measurable dynamical properties. One of the first fruits of such an approach is our recent SLEND and SLEND/KSDFT study on the prediction of absolute ICSs for the one-electron-transfer reactions: $H^+ + B \rightarrow H + B^+$, B = adenine, cytosine, thymine and uracil, at $E_{Lab} =$ 80 keV [32], in good agreement with results from experiments [33] and from CDW and CDW-EIS calculations [8].

This article is organised as follows. In Section 2, we discuss the SLEND theory and our SLEND code CSDyn in the context of the present PCT simulations; in particular, we explain our recent implementation of effective core

potentials (ECPs) in SLEND [4] that facilitates the simulation of large PCT-related systems. In Sections 3 and 4, we present and discuss the results of our SLEND simulations of $H^+ + (H_2O)_{3-4}$ and $H^+ + B$, B = adenine, cytosine, guanine and thymine, at $E_{Lab} = 1$ keV, respectively. Finally, in Section 5, we present some final remarks on the present PCT investigation and some brief advances about our ongoing PCT research with SLEND.

## 2. Methods

### 2.1. Simplest level electron nuclear dynamics (SLEND)

Detailed expositions of the SLEND method [4,12,13,34] and the general END framework [4,12,13,34] are provided in the cited references. Therefore, we present herein a brief account of those methods. As stated earlier, END is a time-dependent, variational, direct and non-adiabatic approach to simulate chemical reactions [4,12,13]. A given END realisation adopts appropriate trial functions for the nuclear $|\Psi_N^{\text{END}}\rangle$ and electronic $|\Psi_e^{\text{END}}\rangle$ wavefunctions comprising the total END wavefunction $|\Psi_{\text{Total}}^{\text{END}}\rangle = |\Psi_N^{\text{END}}\rangle|\Psi_e^{\text{END}}\rangle$. Then, the END dynamical equations are obtained by subjecting $\left|\Psi_{\text{Total}}^{\text{END}}\right\rangle$ to the time-dependent variational principle (TDVP) [35]. In SLEND, where $\left|\Psi_{\text{Total}}^{\text{SLEND}}\right\rangle = |\Psi_N^{\text{SLEND}}\rangle|\Psi_\epsilon^{\text{SLEND}}\rangle$, the nuclear wavefunction $\left|\Psi_N^{\text{SLEND}}\right\rangle$ for a system having $N_N$ nuclei is the product of $3N_N$ frozen, narrow, Gaussian wave packets,

$$\begin{aligned}\left\langle \mathbf{X}\middle|\Psi_N^{\text{SLEND}}(t)\right\rangle &= \langle \mathbf{X}|\mathbf{R}(t),\mathbf{P}(t)\rangle \\ &= \prod_{A=1}^{3N_N}\exp\left\{-\left[\frac{X_A - R_A(t)}{2\Delta R_A}\right]^2 \right. \\ &\quad \left. + iP_A(t)\left[X_A - R_A(t)\right]\right\} \end{aligned} \tag{1}$$

with average positions $\mathbf{R}_A(t)$, average momenta $\mathbf{P}_A(t)$ and widths $\{\Delta R_A\}$. In practice, to lower computational cost, SLEND ultimately adopts the zero-width limit for all the nuclear wave packets in $\left|\Psi_N^{\text{SLEND}}\right\rangle$: $\Delta R_A \to 0\,\forall A$, just before obtaining its dynamical equations. That procedure generates a nuclear classical dynamics as discussed in the following paragraph. Adoption of a nuclear classical dynamics is justified herein given the high energy $E_{Lab} = 1$ keV involved in the present PCT reactions. The SLEND electronic wavefunction $\left|\Psi_e^{\text{SLEND}}\right\rangle$ for a system having $N_e$ electrons is a complex-valued, spin-unrestricted, single-determinantal wavefunction in the Thouless representation [36],

$$\begin{aligned}\left\langle \mathbf{x}\left|\Psi_e^{\text{SLEND}}(t)\right.\right\rangle &= \langle \mathbf{x}\,|\mathbf{z}(t),\mathbf{R}(t)\rangle \\ &= \det\left\{\chi_h\left[\mathbf{x}_h;\mathbf{z}(t),\mathbf{R}(t)\right]\right\}; \\ \chi_h &= \phi_h + \sum_{p=N_e+1}^{K} z_{ph}\phi_p; \quad 1 \le h \le N_e \end{aligned} \tag{2}$$

where $K > N_e$ is the rank (size) of the electronic basis set and $\{\chi_h\}$ are non-orthogonal dynamical spin orbitals (DSOs) [12,13]. The DSOs are linear combinations of orthogonal molecular spin orbitals (MSOs) $\{\phi_h, \phi_p\}$ with complex-valued coefficients $\mathbf{z}(t) = \{z_{ph}(t)\}$; the MSOs split into $N_e$ occupied $\{\phi_h\}$ and $K - N_e$ unoccupied (virtual) $\{\phi_p\}$ MSOs with respect to a reference single-determinantal state $|0\rangle = |\phi_1 \ldots \phi_i \ldots \phi_{N_e}\rangle$. The MSOs are constructed at initial time via a regular self-consistent field (SCF) unrestricted Hartree–Fock (UHF) procedure involving $K$ travelling atomic basis functions centred on the nuclear positions $\mathbf{R}_A(t)$. SLEND employs the somewhat uncommon Thouless single-determinantal wavefunction $\left|\Psi_e^{\text{SLEND}}\right\rangle = |\mathbf{z},\mathbf{R}\rangle$ [36] because it eliminates numerical instabilities in the SLEND dynamical equations (cf. Refs. [4,12] for further details).

The SLEND dynamical equations are obtained by applying the TDVP [35] to the trial function $\left|\Psi_{\text{Total}}^{\text{SLEND}}\right\rangle$ [4,12,13]. The SLEND TDVP procedure involves the following steps: (1) Formulating the quantum Lagrangian $L_{\text{SLEND}} = \left\langle\Psi_{\text{Total}}^{\text{SLEND}}\middle| i\partial/\partial t - \hat{H}\middle|\Psi_{\text{Total}}^{\text{SLEND}}\right\rangle / \left\langle\Psi_{\text{Total}}^{\text{SLEND}}\middle|\,\Psi_{\text{Total}}^{\text{SLEND}}\right\rangle$, (2) applying the zero-width limit to all the nuclear wave packets in $\left|\Psi_{\text{Total}}^{\text{SLEND}}\right\rangle$, and (3) imposing the stationary condition to the quantum action $A_{\text{SLEND}}$: $\delta A_{\text{SLEND}} = \delta\int_{t_1}^{t_2} L_{\text{SLEND}}(t)dt = 0$, with appropriate boundary conditions at the endpoints [4,12,13]. The described procedure generates the SLEND dynamical equations as a set of Euler–Lagrange equations: $d\left(\partial L_{\text{SLEND}}/\partial\dot{q}_i\right)/dt = \partial L_{\text{SLEND}}/\partial q_i$, for the SLEND variational parameters $\{q_i(t)\} = \{R_A(t),\ P_A(t),\ z_{ph}(t),\ z_{ph}^*(t)\}$. The resulting SLEND dynamical equations in matrix form are [4,12,13]

$$\begin{bmatrix} i\mathbf{C} & \mathbf{0} & i\mathbf{C}_\mathbf{R} & \mathbf{0} \\ \mathbf{0} & -i\mathbf{C}^* & -i\mathbf{C}_\mathbf{R}^* & \mathbf{0} \\ i\mathbf{C}_\mathbf{R}^\dagger & -i\mathbf{C}_\mathbf{R}^T & \mathbf{C}_{\mathbf{RR}} & -\mathbf{I} \\ \mathbf{0} & \mathbf{0} & \mathbf{I} & \mathbf{0} \end{bmatrix} \begin{bmatrix} \frac{d\mathbf{z}}{dt} \\ \frac{d\mathbf{z}^*}{dt} \\ \frac{d\mathbf{R}}{dt} \\ \frac{d\mathbf{P}}{dt} \end{bmatrix} = \begin{bmatrix} \frac{\partial E_{\text{Total}}}{\partial \mathbf{z}^*} \\ \frac{\partial E_{\text{Total}}}{\partial \mathbf{z}} \\ \frac{\partial E_{\text{Total}}}{\partial \mathbf{R}} \\ \frac{\partial E_{\text{Total}}}{\partial \mathbf{P}} \end{bmatrix} \tag{3}$$

where $E_{\text{total}}$ is the total energy.

$$\begin{aligned} E_{\text{Total}}&\left[\mathbf{R}(t),\mathbf{P}(t),\mathbf{z}(t),\mathbf{z}(t)^*\right] \\ &= \sum_{A=1}^{N_N}\frac{\mathbf{P}_A^2(t)}{2M_A} + \sum_{A,B>A}^{N_N,N_N}\frac{Z_A Z_B}{|\mathbf{R_A} - \mathbf{R_B}|} \\ &\quad + \frac{\langle\mathbf{z}(t),\mathbf{R}(t)|\,\hat{H}_e\,|\mathbf{z}(t),\mathbf{R}(t)\rangle}{\langle\mathbf{z}(t),\mathbf{R}(t)\,|\,\mathbf{z}(t),\mathbf{R}(t)\rangle} \end{aligned} \tag{4}$$

where $\hat{H}_e$ is the pure electronic Hamiltonian, and $\mathbf{C}$, $\mathbf{C_R}$ and $\mathbf{C_{RR}}$,

$$(\mathbf{C}_{XY})_{ik,jl} = -2\,\mathrm{Im}\frac{\partial^2 \ln S}{\partial X_{ik}\partial Y_{jl}}\bigg|_{\mathbf{R}'=\mathbf{R}};$$
$$\left(\mathbf{C}_{X_{ik}}\right)_{ph} = \frac{\partial^2 \ln S}{\partial z^*_{ph}\partial X_{ik}}\bigg|_{\mathbf{R}'=\mathbf{R}}; \mathbf{C}_{ph,qg} = \frac{\partial^2 \ln S}{\partial z^*_{ph}\partial z_{qg}}\bigg|_{\mathbf{R}'=\mathbf{R}};$$
$$S = \left\langle \mathbf{z}'(t), \mathbf{R}'(t) \mid \mathbf{z}(t), \mathbf{R}(t)\right\rangle \quad (5)$$

are the dynamic metric matrices. $\mathbf{C_R}$ and $\mathbf{C_{RR}}$ can be seen as the SLEND non-adiabatic coupling terms, whose importance for the proper description of non-adiabatic effects is discussed in detail in Ref. [37]. The SLEND equations (3)–(5) express the coupled nuclear and electronic dynamics in a generalised quantum symplectic form [35,38] through the conjugate variables $\{R_A(t), P_A(t)\}$ (nuclear classical) and $\{z_{ph}(t), z^*_{ph}(t)\}$ (electronic quantum), respectively.

In some cases, the application of the SLEND equations (3)–(5) to the full $N_e$ electrons of large systems may become computationally onerous. A way to alleviate such a problem has been recently obtained by our own introduction of the well-known ECP scheme [39] into the SLEND framework [4]. In that SLEND + ECP approach, only the valence electrons are treated explicitly, whereas the core electrons are represented by less computationally expensive pseudo-potentials. The expressions for the SLEND + ECP electronic wavefunction and for the SLEND + ECP dynamical equations have the same mathematical form as those in SLEND but refer only to the valence electrons in the pseudo-potential field simulating the effect of the core electrons (cf. Ref. [4] for more details). Proper use of SLEND + ECP assumes the common chemical notion that core electrons play a quite secondary role to determine chemical structures and chemical reactivity [39]. The correctness of this assumption for reactions at collisions energies $E_{\mathrm{Lab}} \leq$ 100 keV was proven in Refs. [4,40]. SLEND + ECP is employed in the simulations of $H^+ + (H_2O)_4$ at $E_{\mathrm{Lab}} = 1$ keV in Section 3.

### 2.2. *SLEND code: CSDyn*

All of the SLEND simulations presented herein were performed with our code CSDyn (A. Perera, T.V. Grimes and J.A. Morales, CSDyn, Texas Tech University, Lubbock, TX, 2008–2010) developed from the ENDyne 2.7–2.8 codes (E. Deumens *et al.*, ENDyne, Electron Nuclear Dynamics Simulations, Version 2, Release 8, Quantum Theory Project: University of Florida, Gainesville, FL, 1997). Distinctive capabilities of CSDyn include the new SLEND/KSDFT method (already employed in our recent study of the PCT reactions: $H^+ + B \rightarrow H + B^+$, B = adenine, cytosine, thymine and uracil, at $E_{\mathrm{Lab}} = 80$ keV [32]), the new SLEND + ECP method [4], and tools to prepare visualisations of the simulated reactions (cf. Figures 3, 4 and 7–10) via an OpenMP-parallelised C++ code; the latter employs a recursive surface-finding algorithm based on the Marching Cubes algorithm that permits rapid generation of visualisations in POVRay input format.

## 3. Water radiolysis reactions in $H^+ + (H_2O)_{3-4}$ at $E_{\mathrm{Lab}} = 1$ keV

The parameters defining the initial conditions of the nuclei for the SLEND simulations of $H^+ + (H_2O)_{3-4}$ at $E_{\mathrm{Lab}} = 1$ keV are shown in Table 1 and in Figure 2. Those initial conditions are in reference to the laboratory-frame Cartesian coordinate axes. The $(H_2O)_3$ and $(H_2O)_4$ targets are initially optimised in their global-minimum, ground-state, equilibrium geometries at the SCF UHF/6-31G** and SCF UHF + ECP/Stevens-Basch-Krauss-Jasien-Cundari (ECP/SBKJC) levels, respectively. The 6-31G** and ECP/SBKJC basis sets are adopted herein in order to keep the computational cost at a reasonable level during the long dynamical simulations. Table 1 lists the initial positions $\mathbf{R}^i_{\mathrm{H1}}$, $\mathbf{R}^i_{\mathrm{H2}}$, $\mathbf{R}^i_{\mathrm{H4}}$, ..., $\mathbf{R}^i_{\mathrm{O3}}$, $\mathbf{R}^i_{\mathrm{O6}}$, ... of the H and O nuclei in the optimised $(H_2O)_3$ and $(H_2O)_4$ ACs. At the present level of theory, the $(H_2O)_3$ and $(H_2O)_4$ ACs in their global-minimum, ground-state, equilibrium geometries form cyclic structures with all their $H_2O$ molecules acting as both hydrogen-bond donors and acceptors [41] (cf. the first snapshots in Figures 3 and 4); those optimised $(H_2O)_3$ and $(H_2O)_4$ ACs display $C_1$ and $S_4$ symmetries, respectively [41]. For the initial nuclear positions, the $C_1$ $(H_2O)_3$ AC has been placed with its centre of mass at the (0.0, 0.0, 0.0) position and with its pseudo-$C_3$ axis collinear with the $z$-axis; the O nuclei in $(H_2O)_3$ are close to the $xy$ plane (cf. Table 1 and first snapshot of Figure 3). Similarly, the $S_4$ $(H_2O)_4$ AC has been placed with its centre of mass at the (0.0, 0.0, 0.0) position and with its $S_4$ axis collinear with the $z$-axis; the O atoms in $(H_2O)_4$ are alternately above and below the $xy$ plane and close to it (cf. Table 1 and first snapshot of Figure 4). Both ACs are initially at rest: $\mathbf{P}^i_{\mathrm{H1}} = \mathbf{P}^i_{\mathrm{H2}} = \cdots = \mathbf{P}^i_{\mathrm{O3}} = \mathbf{P}^i_{\mathrm{O6}} = \cdots = \mathbf{0}$. All the present SLEND simulations of $H^+ + (H_2O)_{3-4}$ at $E_{\mathrm{Lab}} = 1$ keV start with the ACs in the described initial conditions. The $H^+$ projectile is first prepared with position $\mathbf{R}^0_{\mathrm{H^+}} = (b \geq 0,\ 0,\ 70$ a.u.) and momentum $\mathbf{P}^0_{\mathrm{H^+}} = (0,\ 0,\ p^z_{\mathrm{H^+}} < 0)$ where $b$ is the projectile's impact parameter and $p^z_{\mathrm{H^+}}$ corresponds to a kinetic energy $E_{\mathrm{Lab}} = 1$ keV. The definite initial conditions of the $H^+$ projectile $\mathbf{R}^i_{\mathrm{H^+}}$ and $\mathbf{P}^i_{\mathrm{H^+}}$ are obtained by rotating $\mathbf{R}^0_{\mathrm{H^+}}$ and $\mathbf{P}^0_{\mathrm{H^+}}$ by the Euler angles $0^\circ \leq \alpha \leq 180^\circ$, $0^\circ \leq \beta < 360^\circ$ and $0^\circ \leq \gamma < 360^\circ$ in the $y - z - z$ convention and operated in the order: $\gamma$, $\alpha$, and $\beta$ (cf. Figure 2); these operations define a relative projectile-target orientation denoted as $\alpha - \beta - \gamma$. The $(\alpha, \beta)$ direction defines a particular axis of incidence for $H^+$ projectiles initially distributed around it with impact parameters $b's$ and azimuthal angles $\gamma's$.

Table 1. Optimised Cartesian coordinates of the nuclei in the water trimer, $(H_2O)_3$, and tetramer, $(H_2O)_4$, at the UHF/6-31G** and UHF + ECP/SBKJC levels, respectively. Values are in atomic units.

| | $(H_2O)_3$ | | | $(H_2O)_4$ | | |
|---|---|---|---|---|---|---|
| Nucleus label | *X* position | *Y* position | *Z* position | *X* position | *Y* position | *Z* position |
| H1 | −1.4146966633 | 1.9138718063 | 0.2397594558 | 1.4263757722 | −2.6086950758 | −0.0516569921 |
| H2 | −0.3708957686 | 4.1776538871 | −1.1741890740 | 0.1134060670 | −5.0757815508 | −1.2631420624 |
| O3 | −0.0812256578 | 3.1200018907 | 0.2308447532 | −0.1282351144 | −3.5633241123 | −0.3125276949 |
| H4 | 2.3728005887 | 0.2683448594 | −0.1011891389 | −2.6086950758 | −1.4263757722 | 0.0516569921 |
| H5 | 3.8690054757 | −1.8107757706 | 1.1902855365 | −5.0757815508 | −0.1134060670 | 1.2631420624 |
| O6 | 2.7618978152 | −1.4857612475 | −0.1672089337 | −3.5633241123 | 0.1282351144 | 0.3125276949 |
| H7 | −0.9870216715 | −2.2094903714 | −0.2502099194 | 2.6086950758 | 1.4263757722 | 0.0516569921 |
| H8 | −3.4531144306 | −2.5401118385 | 1.1849090996 | 5.0757815508 | 0.1134060670 | 1.2631420624 |
| O9 | −2.6816851832 | −1.6216069120 | −0.1322754555 | 3.5633241123 | −0.1282351144 | 0.3125276949 |
| H10 | | | | −1.4263757722 | 2.6086950758 | −0.0516569921 |
| H11 | | | | −0.1134060670 | 5.0757815508 | −1.2631420624 |
| O12 | | | | 0.1282351144 | 3.5633241123 | −0.3125276949 |

All the present water radiolysis simulations start with the same initial conditions for the ACs according to Table 1 and with varying initial conditions for the $H^+$ projectile: $\alpha - \beta - \gamma$ and $b$. However, when possible, the symmetry of the AC is taken into account to avoid replicating equivalent relative orientations $\alpha - \beta - \gamma$. With the totally asymmetric $C_1$ $(H_2O)_3$ AC, no replication of equivalent orientations is possible; therefore, the variations of the angles $\alpha$, $\beta$ and $\gamma$ with that target AC are over their full ranges; those variations are in independent steps $\Delta\alpha = \Delta\beta = \Delta\gamma = 45^\circ$. This procedure generates 208 non-equivalent $\alpha - \beta - \gamma$ orientations. With the more symmetric $S_4$ $(H_2O)_4$ AC, replications of equivalent orientations are possible; therefore, the variations of the $\alpha$, $\beta$ and $\gamma$ angles are restricted. By adopting again independent steps $\Delta\alpha = \Delta\beta = \Delta\gamma = 45^\circ$, the angles $\alpha$, $\beta$ and $\gamma$ are varied as follows: $0^\circ - 0^\circ - \gamma'$ with $0^\circ \leq \gamma' \leq 135^\circ$; and $45^\circ - 0^\circ - \gamma''$, $45^\circ - 45^\circ - \gamma''$, $45^\circ - 90^\circ - \gamma''$, $90^\circ - 0^\circ - \gamma''$ and $90^\circ - 45^\circ - \gamma''$ with $0^\circ \leq \gamma'' \leq 315^\circ$. This procedure generates 44 non-equivalent $\alpha - \beta - \gamma$ orientations: The symmetry of $(H_2O)_4$ drastically reduces the number of non-equivalent orientations. Finally, the impact parameter $b$ is varied in steps $\Delta b = 0.2$ a.u. over the ranges $0 \leq b \leq 4.4$ a.u. in $H^+ + (H_2O)_3$ and $0 \leq b \leq 6.0$ a.u. in $H^+ + (H_2O)_4$, respectively. The total described variations in $\alpha - \beta - \gamma$ and $b$ originate 4602 and 1326 individual, non-equivalent simulations for the $H^+ + (H_2O)_3$ and $H^+ + (H_2O)_4$ collisions, respectively.

From the described initial conditions, the SLEND simulations of $H^+ + (H_2O)_{3-4}$ at $E_{Lab} = 1$ keV are carried out for total run times of at least 1040 a.u. (=25.16 fs) and 2000 a.u. (=48.38 fs), respectively. Those run times allow

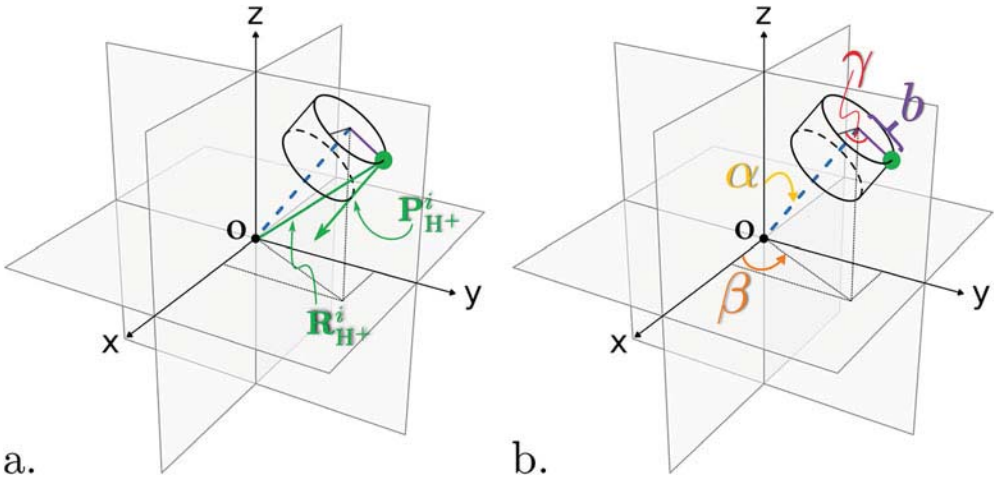


Figure 2. Initial position $\mathbf{R}^i_{H^+}$ and initial momentum $\mathbf{P}^i_{H^+}$ (panel a) of a $H^+$ projectile (green sphere) corresponding to Euler angles $\alpha$, $\beta$ and $\gamma$ and to an impact parameter $b$ (panel b). A given water cluster target (not depicted for clarity's sake) is placed with its centre of mass on the axes' origin O (see text and Table 1 for further details).

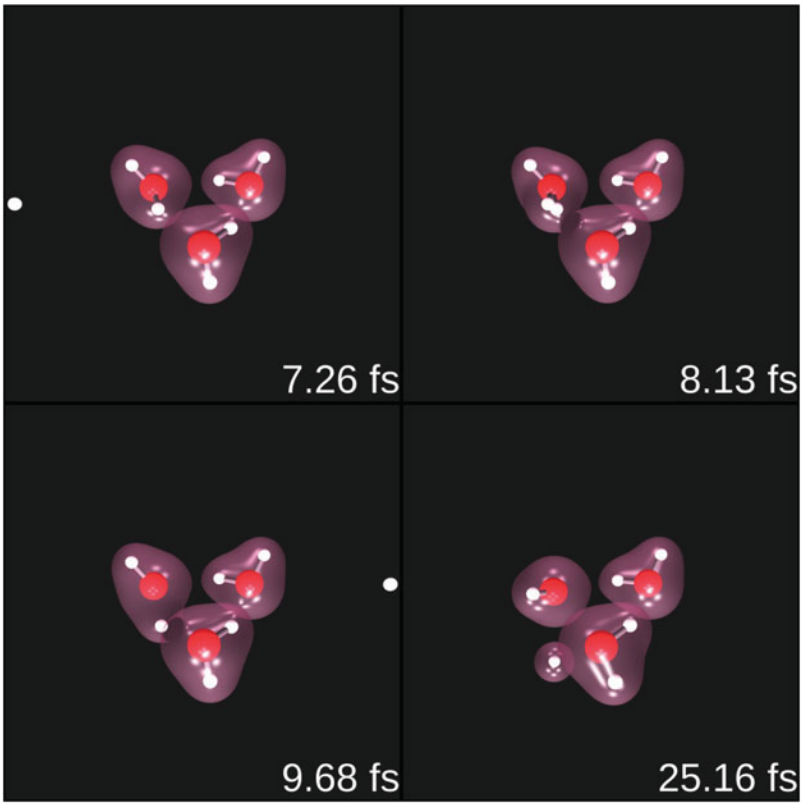


Figure 3. SLEND/6-31G** simulation of $H^+ + (H_2O)_3$ at $E_{Lab} = 1$ keV from orientation $\alpha$–$\beta$–$\gamma = 90°$–$0°$–$135°$ and impact parameter $b = 0.2$ a.u. leading to $H^{q_H}$ and $OH^{q_{OH}}$ FF [cf. Equation (7)].



for final projectile-target (products) separations of at least 70 a.u., which is equivalent to the minimal initial projectile-target (reactants) separation of 70 a.u. When a SLEND simulation is complete, auxiliary codes in the CSDyn package analyse the predicted final state to characterise the simulated process (e.g. projectile scattering (PS), fragments formation (FF), etc., cf. the following paragraphs). After that, other auxiliary codes in the CSDyn package calculate various dynamical properties (e.g. ICSs) from the SLEND simulation data as explained in the following paragraphs.

Present SLEND simulations of $H^+ + (H_2O)_{3-4}$ at $E_{Lab} = 1$ keV predicted the following two main processes within the stipulated run times:

- PS;

$$\begin{aligned} H^+ + (H_2O)_3 &\rightarrow H^{q_P} + (H_2O)_3^{q_{AC}}; \quad q_P + q_{AC} = +1 \\ H^+ + (H_2O)_4 &\rightarrow H^{q_P} + (H_2O)_4^{q_{AC}}; \quad q_P + q_{AC} = +1 \end{aligned} \tag{6}$$

a non-reactive nuclear process where the incoming projectile $H^+$ is scattered off as the outgoing projectile $H^{q_P}$ after colliding with the AC and leaving behind a formed $(H_2O)_{3-4}^{q_{AC}}$ AC ion undergoing vibrational, rotational and electronic excitations.

- $H^{q_H}$ and $OH^{q_{OH}}$ FF;

$$\begin{aligned} H^+ + (H_2O)_3 &\rightarrow H^{q_P} + H^{q_H} + OH^{q_{OH}} (H_2O)_2; \\ & \qquad q_P + q_H + q_{OH} = +1 \\ H^+ + (H_2O)_4 &\rightarrow H^{q_P} + H^{q_H} + OH^{q_{OH}} (H_2O)_3; \\ & \qquad q_P + q_H + q_{OH} = +1 \end{aligned} \tag{7}$$

a reactive nuclear process where the incoming projectile $H^+$ is scattered off as the outgoing projectile $H^{q_P}$ after colliding with the AC target and producing the $OH^{q_{OH}}$ and $H^{q_H}$ fragments from one of the $H_2O$ molecules in the AC.

In all the predicted $H^{q_H}$ and $OH^{q_{OH}}$ FF, the $H^{q_H}$ and $OH^{q_{OH}}$ fragments are formed from the $H_2O$ molecule directly hit by the incoming projectile $H^+$, and not from an $H_2O$ molecule distant from that impact area that could have been dissociated by the impact momentum ('shock wave') transmitted through the AC. Also, in all the predicted $H^{q_H}$ and $OH^{q_{OH}}$ FF, the $OH^{q_{OH}}$ fragment ends up solvated in the final AC, $OH^{q_{OH}} (H_2O)_{2-3}$, while the outgoing projectile $H^{q_P}$ and the $H^{q_H}$ fragment depart considerably from the

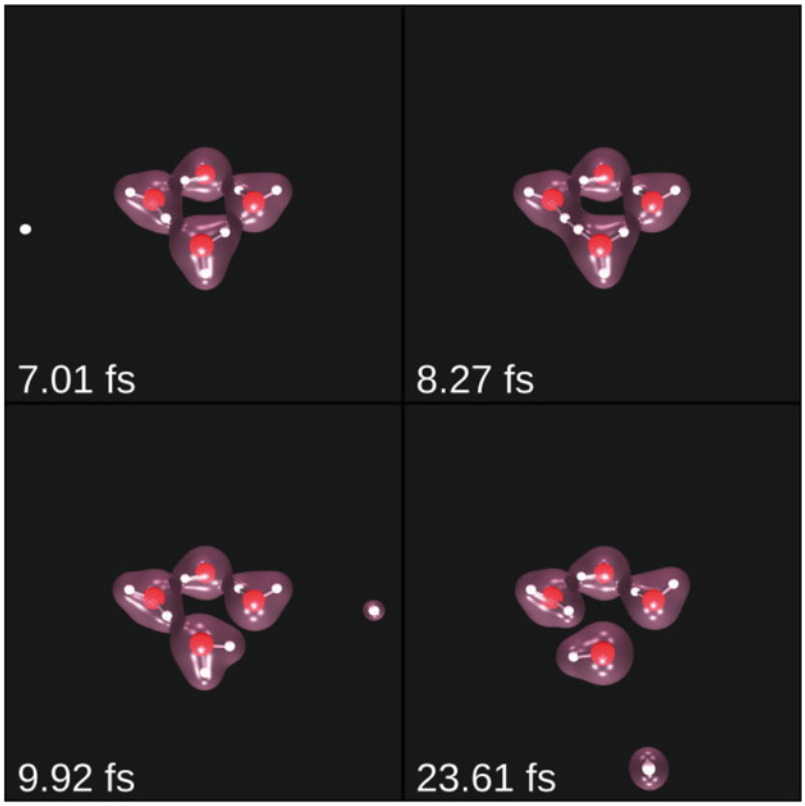


Figure 4. SLEND + ECP/SBKJC simulation of $H^+ + (H_2O)_4$ at $E_{Lab} = 1$ keV from orientation $\alpha$–$\beta$–$\gamma = 90°$–$0°$–$90°$ and impact parameter $b = 2.4$ a.u. leading to $H^{q_H}$ and $OH^{q_{OH}}$ FF [cf. Equation (7)].

final AC. It is worth noticing that for $H^+ + (H_2O)_4$, $H_2$ and O formation [$H^+ + (H_2O)_4 \rightarrow H_2 + O + (H_2O)_3$] were also observed in one simulation with initial orientation $\alpha - \beta - \gamma = 0° - 0° - 0°$ and impact parameter $b =$ 3.6 a.u. (a highly reactive O fragment can have a strong deleterious effect on DNA).

Figure 3 shows a sequence of four snapshots from a SLEND/6-31G** simulation of $H^+ + (H_2O)_3$ from the initial orientation $\alpha - \beta - \gamma = 90° - 0° - 135°$ and $b =$ 0.2 a.u. that leads to a $H^{q_H}$ and $OH^{q_{OH}}$ FF. Figure 4 shows an equivalent sequence for a SLEND + ECP/SBKJC simulation of $H^+ + (H_2O)_4$ from the initial orientation $\alpha - \beta - \gamma = 90° - 0° - 90°$ and $b = 2.4$ a.u. that also leads to a $H^{q_H}$ and $OH^{q_{OH}}$FF. In those figures, white and red spheres represent the classical H and O nuclei, respectively, while the purple surfaces enclosing those nuclei represent electron density isosurfaces. Inspection of those isosurfaces in Figure 3 for the $H^+ + (H_2O)_3$ case reveals that the final outgoing projectile $H^{q_P}$ (snapshot at 9.68 fs) carries a minimal electron density with it, that final projectile being mostly an $H^+$ with a Mulliken charge $q_P = +0.89$ (cf. Table 2; this final projectile's density is not clearly visible in Figure 3 due to its plotting settings). Additionally, the $H^{q_H}$ fragment (snapshot at 25.16 fs) carries considerable electron density with it, that fragment being mostly an H atom with a Mulliken charge $q_H = +0.12$ (cf. Table 2). Similarly, the same inspection in Figure 4 for the $(H_2O)_4$ case reveals that the final outgoing projectile $H^{q_P}$ (snapshot at 9.92 fs) carries some electron density with it, that final projectile having a Mulliken charge $q_P = +0.66$ (cf. Table 3), while the $H^{q_H}$ fragment (snapshot at 23.61 fs) carries considerable electron density with it, having a Mulliken charge $q_H = +0.35$ (cf. Table 3). A further analysis of the final charges in $H^{q_H}$ and $OH^{q_{OH}}$ FF is given below, following the discussion of Figures 5 and 6.

Aside from the described processes, the present SLEND simulations did not predict any of the other hypothetical PCT water radiolysis reactions discussed in Section 1 (e.g. $H_3O^+$ formation: $H^+ + (H_2O)_{3-4} \rightarrow H_3O^+ + (H_2O)_{2-3}$, etc.). However, it is quite possible that those additional PCT water radiolysis reactions will be predicted by SLEND if additional simulations are run by increasing the number of the initial condition grid points $\alpha - \beta - \gamma$ and $b$ from those employed currently and/or other collision energies $E_{Lab}'s$ are explored. In the present simulations, PS completely predominates over $H^{q_H}$ and $OH^{q_{OH}}$ FF. Out of the 4602 simulations to model $H^+ + (H_2O)_3$, only 75 simulations (1.63%) resulted in $H^{q_H}$ and $OH^{q_{OH}}$FF; the rest (98.37%) resulted in PS. Similarly, out of the 1326 simulations to model $H^+ +$ $(H_2O)_4$, only 40 simulations (3.02%) resulted in $H^{q_H}$ and

Table 2. Initial $\alpha$–$\beta$–$\gamma$ orientations and impact parameters $b$ of all the SLEND/6-31G** simulations of $H^+ + (H_2O)_3$ at $E_{Lab} =$ 1 keV predicting $H^{q_H}$ and $OH^{q_{OH}}$ FF, Equation (7), along with the $H^{q_H}$ nucleus label from Table 1, and fragments' Mulliken charges. * indicates the simulation in Figure 3.

| $\alpha$ | $\beta$ | $\gamma$ | $b$ | $H^{q_H}$ nuc. label | $q_H$ | $q_P$ | $q_{OH}$ |
|---|---|---|---|---|---|---|---|
| 45 | 0 | 315 | 2.4 | H5 | 0.18 | 0.76 | 0.05 |
| 45 | 0 | 315 | 2.6 | H5 | 0.21 | 0.77 | 0.02 |
| 45 | 0 | 315 | 2.8 | H5 | 0.02 | 0.71 | 0.27 |
| 45 | 45 | 90 | 2.2 | H1 | 0.17 | 0.79 | 0.04 |
| 45 | 45 | 270 | 4.0 | H5 | 0.19 | 0.79 | 0.01 |
| 45 | 45 | 315 | 1.8 | H4 | 0.20 | 0.67 | 0.14 |
| 45 | 45 | 315 | 2.2 | H4 | 0.08 | 0.87 | 0.05 |
| 45 | 90 | 135 | 1.6 | H7 | 0.07 | 0.74 | 0.18 |
| 45 | 90 | 270 | 2.4 | H4 | −0.09 | 0.79 | 0.31 |
| 45 | 225 | 135 | 2.0 | H4 | 0.21 | 0.57 | 0.22 |
| 45 | 270 | 90 | 2.2 | H4 | 0.15 | 0.61 | 0.24 |
| 45 | 270 | 90 | 2.4 | H4 | 0.73 | 0.64 | −0.36 |
| 45 | 270 | 90 | 2.6 | H1 | 0.02 | 0.52 | 0.46 |
| 45 | 270 | 225 | 2.0 | H1 | 0.20 | 0.83 | −0.03 |
| 45 | 270 | 225 | 2.2 | H1 | 0.19 | 0.80 | 0.01 |
| 90 | 0 | 45 | 0.2 | H4 | 0.65 | 0.82 | −0.47 |
| 90 | 0 | 45 | 0.4 | H4 | 0.17 | 0.85 | −0.02 |
| 90 | 0 | 90 | 0.2 | H4 | 0.46 | 0.88 | −0.34 |
| 90 | 0 | 90 | 0.4 | H4 | 0.27 | 0.80 | −0.07 |
| 90 | 0 | 90 | 2.0 | H1 | 0.07 | 0.73 | 0.21 |
| 90 | 0 | 135 | 0.2* | H4 | 0.12 | 0.89 | −0.01 |
| 90 | 45 | 270 | 0.6 | H7 | 0.33 | 0.60 | 0.06 |
| 90 | 45 | 270 | 0.8 | H7 | 0.04 | 0.63 | 0.33 |
| 90 | 45 | 270 | 1.0 | H7 | 0.02 | 0.72 | 0.26 |
| 90 | 45 | 270 | 1.4 | H4 | 0.22 | 0.73 | 0.04 |
| 90 | 45 | 270 | 1.6 | H4 | 0.73 | 0.75 | −0.48 |
| 90 | 90 | 90 | 0.8 | H7 | 0.26 | 0.70 | 0.04 |
| 90 | 90 | 90 | 1.0 | H7 | 0.73 | 0.70 | −0.43 |
| 90 | 90 | 90 | 1.4 | H1 | 0.18 | 0.70 | 0.12 |
| 90 | 90 | 270 | 2.2 | H4 | 0.16 | 0.86 | −0.02 |
| 90 | 90 | 270 | 2.4 | H4 | 0.22 | 0.71 | 0.07 |
| 90 | 135 | 225 | 0.6 | H1 | 0.31 | 0.84 | −0.15 |
| 90 | 135 | 225 | 1.8 | H5 | −0.06 | 0.93 | 0.13 |
| 90 | 135 | 270 | 0.4 | H1 | 0.23 | 0.86 | −0.10 |
| 90 | 135 | 270 | 0.6 | H4 | 0.13 | 0.80 | 0.07 |
| 90 | 135 | 270 | 1.0 | H4 | 0.10 | 0.72 | 0.19 |
| 90 | 135 | 270 | 1.2 | H4 | −0.03 | 0.58 | 0.45 |
| 90 | 180 | 270 | 0.2 | H4 | 0.27 | 0.73 | 0.00 |
| 90 | 180 | 270 | 0.4 | H4 | 0.14 | 0.76 | 0.09 |
| 90 | 180 | 270 | 2.0 | H1 | 0.17 | 0.73 | 0.11 |
| 90 | 180 | 315 | 0.2 | H4 | 0.72 | 0.62 | −0.34 |
| 90 | 180 | 315 | 0.4 | H4 | 0.19 | 0.78 | 0.03 |
| 90 | 225 | 90 | 0.8 | H7 | 0.01 | 0.75 | 0.25 |
| 90 | 225 | 90 | 1.2 | H4 | 0.11 | 0.79 | 0.10 |
| 90 | 225 | 90 | 1.4 | H4 | 0.26 | 0.80 | −0.07 |
| 90 | 225 | 90 | 1.6 | H4 | 0.55 | 0.70 | −0.25 |
| 90 | 225 | 90 | 3.0 | H5 | 0.35 | 0.79 | −0.14 |
| 90 | 270 | 90 | 2.8 | H5 | 0.26 | 0.81 | −0.07 |
| 90 | 270 | 270 | 0.2 | H2 | 0.13 | 0.66 | 0.20 |
| 90 | 270 | 270 | 1.2 | H1 | 0.36 | 0.50 | 0.15 |
| 90 | 270 | 270 | 1.4 | H1 | 0.29 | 0.69 | 0.02 |
| 90 | 270 | 270 | 1.6 | H1 | −0.09 | 0.70 | 0.39 |
| 90 | 270 | 270 | 2.2 | H1 | 0.20 | 0.46 | 0.35 |
| 90 | 315 | 90 | 0.8 | H5 | 0.40 | 0.66 | −0.06 |
| 90 | 315 | 90 | 1.4 | H4 | 0.25 | 0.80 | −0.05 |
| 90 | 315 | 90 | 1.6 | H4 | 0.37 | 0.72 | −0.09 |
| 90 | 315 | 90 | 1.8 | H4 | 0.39 | 0.79 | −0.18 |
| 90 | 315 | 135 | 1.8 | H5 | 0.24 | 0.68 | 0.07 |
| 90 | 315 | 135 | 2.0 | H5 | 0.26 | 0.67 | 0.06 |
| 90 | 315 | 270 | 2.4 | H7 | −0.08 | 0.71 | 0.36 |
| 135 | 45 | 225 | 1.8 | H4 | 0.38 | 0.58 | 0.04 |
| 135 | 45 | 225 | 2.0 | H4 | 0.36 | 0.55 | 0.08 |
| 135 | 90 | 135 | 2.0 | H1 | 0.19 | 0.83 | −0.01 |
| 135 | 90 | 135 | 2.2 | H4 | 0.27 | 0.77 | −0.04 |
| 135 | 90 | 270 | 2.2 | H4 | 0.25 | 0.73 | 0.02 |
| 135 | 90 | 270 | 2.4 | H4 | 0.44 | 0.44 | 0.11 |
| 135 | 225 | 45 | 1.8 | H4 | 0.21 | 0.78 | 0.01 |
| 135 | 225 | 45 | 2.2 | H4 | 0.08 | 0.83 | 0.09 |
| 135 | 225 | 90 | 4.0 | H5 | 0.22 | 0.78 | 0.01 |
| 135 | 225 | 270 | 2.2 | H1 | 0.21 | 0.83 | −0.04 |
| 135 | 270 | 90 | 2.4 | H4 | 0.17 | 0.79 | 0.04 |
| 135 | 270 | 225 | 1.6 | H7 | 0.09 | 0.64 | 0.27 |
| 135 | 270 | 315 | 1.6 | H1 | 0.10 | 0.76 | 0.15 |
| 135 | 270 | 315 | 2.0 | H1 | 0.21 | 0.74 | 0.05 |
| 135 | 315 | 45 | 4.0 | H2 | 0.09 | 0.47 | 0.44 |
| Mean charges | | | | | 0.22 | 0.73 | 0.05 |

$OH^{q_{OH}}$FF, while the remaining 1286 simulations (96.98%) resulted in PS.

In the case of the predicted $H^{q_H}$ and $OH^{q_{OH}}$FF, it is important to know its occurrence and the charges $q_P$, $q_H$ and $q_{OH}$ of its products $H^{q_P}$, $H^{q_H}$ and $OH^{q_{OH}}$ $(H_2O)_{2-3}$ as a function of the initial conditions $\alpha - \beta - \gamma$ and $b$. Table 2 lists all the initial conditions $\alpha - \beta - \gamma$ and $b$ in the $H^+ + (H_2O)_3$ simulations that lead to $H^{q_H}$ and $OH^{q_{OH}}$FF along with the Mulliken charges $q_P$, $q_H$ and $q_{OH}$ of the products and the nucleus label identifying the ejected $H^{q_H}$ fragment according to Table 1 (i.e. the initial nucleus label H1, H2, ... or H8 therein). Additionally, Table 2 contains the mean Mulliken charges $\bar{q}_P$, $\bar{q}_H$ and $\bar{q}_{OH}$ from all the predicted $H^{q_H}$ and $OH^{q_{OH}}$ FF. Table 3 lists the same information for the $H^+ + (H_2O)_4$ simulations. Initial conditions not listed in Table 2 and 3 lead to PS by default.

Selected data from Table 2 and 3 can also be visualised using the polar-type maps in Figures 5 and 6. Figure 5 shows the occurrence of $OH^{q_{OH}}$ fragments from all the $H^+ + (H_2O)_3$ simulations initiated with $\alpha = 90°$. In that figure, circular sectors are demarcated by the successive values of $\beta$ – 0° and 45°, 45° and 90°, etc. – and assigned to the lower demarcating value of $\beta$. Within each sector, the polar angular coordinate represents $\gamma$ in its whole range, $0° \le \gamma \le 360°$, as indicated by a curved arrow, while the radial coordinate represents $b$ in its entire range, $0 \le b \le b_{max}$, as indicated by its printed values – 1 a.u., 2. a.u., etc. – along a radius. For example, the first circular sector is demarcated by $\beta = 0°$ and $\beta = 45°$, and corresponds to initial orientations with $\beta = 0°$; all points within that sector pertain to initial orientations $\alpha - \beta - \gamma = 90° - 0° - \gamma$,

Table 3. Non-equivalent initial $\alpha$–$\beta$–$\gamma$ orientations and impact parameters $b$ of all the SLEND/SBKJC simulations of $H^+ + (H_2O)_4$ at $E_{Lab} = 1$ keV leading to $H^{q_H}$ and $OH^{q_{OH}}$ FF, Equation (7), along with the $H^{q_H}$ nucleus label from Table 1, and fragments' Mulliken charges. * indicates the simulation in Figure 4.

| $\alpha$ | $\beta$ | $\gamma$ | $b$ | $H^{q_H}$ nuc. label | $q_H$ | $q_P$ | $q_{OH}$ |
|---|---|---|---|---|---|---|---|
| 0 | 0 | 0 | 4.8 | H8 | 0.24 | 0.87 | −0.11 |
| 0 | 0 | 0 | 5.0 | H8 | 0.30 | 0.74 | −0.03 |
| 0 | 0 | 0 | 5.2 | H8 | 0.59 | 0.54 | −0.13 |
| 0 | 0 | 90 | 4.8 | H11 | 0.01 | 0.73 | 0.26 |
| 0 | 0 | 90 | 5.0 | H11 | 0.16 | 0.63 | 0.21 |
| 0 | 0 | 90 | 5.2 | H11 | 0.30 | 0.41 | 0.29 |
| 45 | 0 | 0 | 2.4 | H1 | 0.00 | 0.61 | 0.39 |
| 45 | 0 | 0 | 2.4 | H8 | −0.15 | 0.61 | 0.54 |
| 45 | 0 | 0 | 2.6 | H8 | −0.29 | 0.73 | 0.57 |
| 45 | 0 | 0 | 2.8 | H8 | 0.39 | 0.63 | −0.02 |
| 45 | 0 | 45 | 2.4 | H7 | 0.05 | 0.72 | 0.23 |
| 45 | 0 | 180 | 4.4 | H5 | 0.32 | 0.50 | 0.18 |
| 45 | 0 | 180 | 4.6 | H5 | 0.10 | 0.64 | 0.26 |
| 45 | 45 | 45 | 4.8 | H11 | 0.24 | 0.54 | 0.22 |
| 45 | 45 | 45 | 5.0 | H11 | 0.08 | 0.76 | 0.16 |
| 45 | 45 | 135 | 4.8 | H5 | 0.25 | 0.52 | 0.23 |
| 45 | 45 | 135 | 5.0 | H5 | 0.19 | 0.72 | 0.09 |
| 45 | 90 | 0 | 4.2 | H11 | 0.34 | 0.40 | 0.26 |
| 45 | 90 | 0 | 4.4 | H11 | 0.26 | 0.36 | 0.37 |
| 45 | 90 | 0 | 4.6 | H11 | 0.34 | 0.72 | −0.06 |
| 45 | 90 | 180 | 2.2 | H1 | 0.06 | 0.75 | 0.19 |
| 90 | 0 | 90 | 1.2 | H7 | 0.01 | 0.72 | 0.28 |
| 90 | 0 | 90 | 1.4 | H7 | 0.41 | 0.77 | −0.19 |
| 90 | 0 | 90 | 1.6 | H7 | 0.12 | 0.73 | 0.15 |
| 90 | 0 | 90 | 2.4* | H10 | 0.35 | 0.66 | −0.01 |
| 90 | 0 | 90 | 2.6 | H10 | 0.27 | 0.62 | 0.11 |
| 90 | 0 | 180 | 0.8 | H8 | 0.00 | 0.56 | 0.45 |
| 90 | 0 | 180 | 1.0 | H8 | 0.01 | 0.78 | 0.21 |
| 90 | 0 | 180 | 1.4 | H8 | 0.21 | 0.69 | 0.11 |
| 90 | 0 | 225 | 0.4 | H7 | 0.06 | 0.64 | 0.30 |
| 90 | 0 | 270 | 1.2 | H4 | 0.30 | 0.64 | 0.06 |
| 90 | 0 | 270 | 1.4 | H4 | 0.24 | 0.71 | 0.05 |
| 90 | 0 | 270 | 1.6 | H4 | 0.18 | 0.73 | 0.10 |
| 90 | 0 | 270 | 2.4 | H1 | 0.31 | 0.75 | −0.06 |
| 90 | 0 | 270 | 2.6 | H1 | 0.22 | 0.77 | 0.01 |
| 90 | 45 | 90 | 0.6 | H4 | 0.39 | 0.77 | −0.16 |
| 90 | 45 | 90 | 0.8 | H4 | 0.22 | 0.76 | 0.02 |
| 90 | 45 | 90 | 1.0 | H4 | 0.64 | 0.62 | −0.26 |
| 90 | 45 | 90 | 1.2 | H4 | 0.29 | 0.73 | −0.02 |
| 90 | 45 | 270 | 0.8 | H7 | 0.33 | 0.71 | −0.04 |
| Mean charges | | | | | 0.20 | 0.66 | 0.13 |

$0 \leq \gamma < 360^\circ$, with $\gamma$ varying in its full range counterclockwise from the sector's boundary at $\beta = 0^\circ$ to the other boundary at $\beta = 45^\circ$; the radial coordinate gives the value of $b$. The presence of a coloured speck in a point corresponding to the initial conditions $90^\circ$–$\beta$–$\gamma$ and $b$ indicates that a $OH^{q_{OH}}$ fragment was formed in the simulation from these conditions, whereas the absence of a coloured speck indicates a PS for that simulation. The colour of the speck corresponds to the Mulliken charge of the $OH^{q_{OH}}$ fragment, $q_{OH}$, according to the colour scale at Figure 5's base. Figure 6 shows the same information for the $H^+ + (H_2O)_4$ system for all the processes starting with $\alpha = 90^\circ$.

The discussed Mulliken charges $q_P$, $q_H$ and $q_{AC}$ for the $H^{q_H}$ and $OH^{q_{OH}}$ FF products (cf. Table 2 and 3) result from applying the Mulliken population analysis to the final electron density $\rho_e^f(x)$ corresponding to the final electronic wavefunction $\Psi_e^f$. In all the $H^{q_H}$ and $OH^{q_{OH}}$ FF simulations, the three predicted products ($H^{q_P}$, $H^{q_H}$ and $OH^{q_{OH}}(H_2O)_{2-3}$) end up well separated among themselves at final time. In that condition, if $\Psi_e^f$ corresponds to a single SCF UHF state (e.g. the system's SCF UHF ground state), then the Mulliken charges of those products will assume integer values due to the appropriate asymptotic behaviour of the unrestricted single-determinantal wavefunction $\Psi_e^f$. However, due to the non-adiabatic nature of SLEND, $\Psi_e^f$ is in general a superposition of several SCF UHF states corresponding to various products' channels [42] (e.g. $H^+ + (H_2O)_{3-4} \rightarrow H^{q_P=+1} + H^{q_H=0} + OH^{q_{OH}=0}(H_2O)_{2-3}$, or $\rightarrow H^{q_P=+1} + H^{q_H=+1} + OH^{q_{AC}=-1}(H_2O)_{2-3}$, or $\rightarrow H^{q_P=0} + H^{q_H=+1} + OH^{q_{AC}=0}(H_2O)_{2-3}$, etc.), each channel state occurring with some probability [42]. While the products' Mulliken charges in each channel state are integer-valued, the Mulliken charges $q_P$, $q_H$ and $q_{AC}$ from $\Psi_e^f$ are an 'average' over those channel states' charges and may, therefore, assume non-integer values [42]. Inspection of the charges $q_P$, $q_H$ and $q_{AC}$ and their mean values $\bar{q}_P$, $\bar{q}_H$ and $\bar{q}_{OH}$ in Table 2 and 3 reveals that in most $H^{q_H}$ and $OH^{q_{OH}}$ FF predictions, those charges assume non-integer values close to the integer values $q_P = +1$, $q_H = 0$ and $q_{OH} = 0$, respectively. That fact indicates that SLEND predicts the products' channel $H^{q_P=+1} + H^{q_H=0} + OH^{q_{OH}=0}(H_2O)_{2-3}$ as the most probable outcome during $H^{q_H}$ and $OH^{q_{OH}}$ FF processes. In other words, SLEND predicts that the formation of solvated OH· radicals $OH \cdot (H_2O)_{2-3}$ is the predominant process during $H^{q_H}$ and $OH^{q_{OH}}$ FF in the present systems. As discussed in Section 1, the OH· radicals are responsible for extensive DNA damage in PCT (cf. Figure 1). A more precise quantification of the probabilities for each channel obtained by projecting $\Psi_e^f$ onto the different channel states (cf. Ref. [42]) will be soon presented in a subsequent publication [43].

The $H^{q_H}$ and $OH^{q_{OH}}$ FF process can be quantified by calculating its total ICS. In the present SLEND framework and from the discussed initial conditions, the total ICS $\sigma_R$ for a reactive process $R$ is [32,40]

$$\sigma_R = \frac{1}{4\pi}\int_0^\infty \int_0^\pi \int_0^{2\pi} \int_0^{2\pi} b P_R(\alpha, \beta, \gamma, b)\, db \times \sin\alpha d\alpha d\beta d\gamma \quad (8)$$

where $P_R(\alpha, \beta, \gamma, b)$ is the probability for the reactive process $R$ to happen from the initial conditions $\alpha - \beta - \gamma$ and $b$. Note that for atom–atom collisions involving

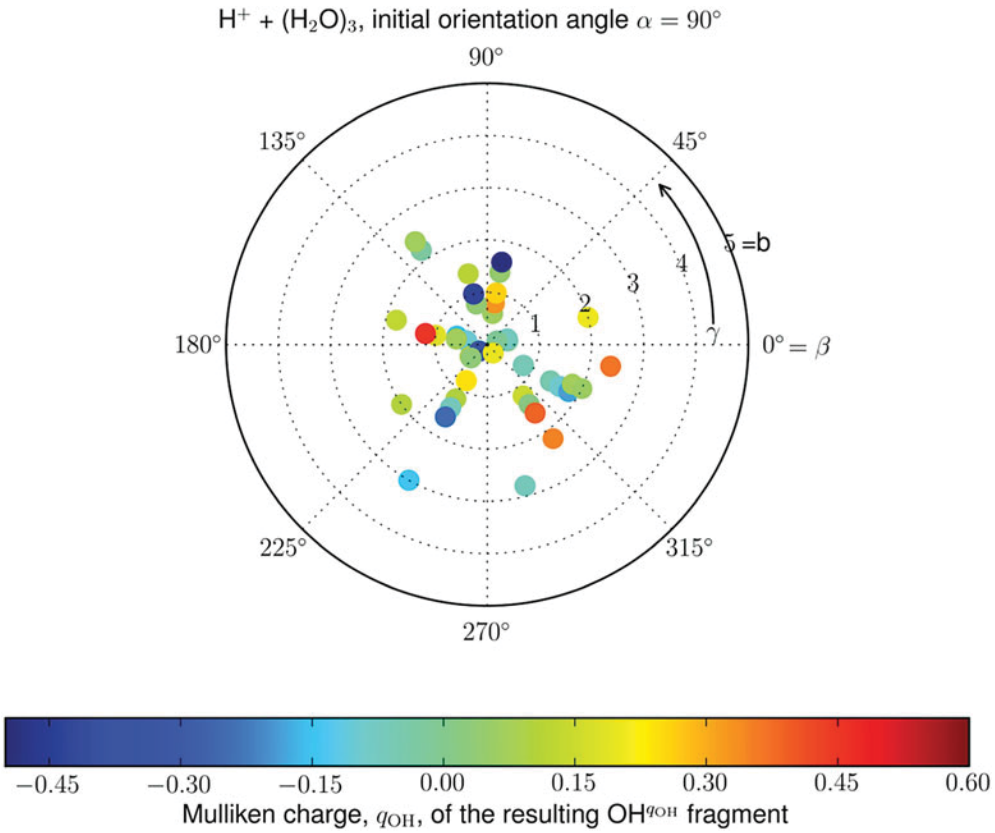


Figure 5. Occurrence and charge, $q_{OH}$, of $OH^{q_{OH}}$ in the $H^+ + (H_2O)_3$ simulation at $E_{Lab} = 1$ keV from $\alpha = 90°$. Circular sectors delimit varying discrete values of $\beta$. Within each sector, $\gamma$ varies in its whole range as the polar angle from one sector's boundary to another, and the radial coordinate is the impact parameter $b$ (see text for further details).



spherical potentials, Equation (8) reduces to the familiar ICS expression $\sigma_R$: $P_R(\alpha, \beta, \gamma, b) \rightarrow P_R(b) \Rightarrow \sigma_R = 2\pi \int_0^\infty b P_R(b)\, db$ [44]. In the present simulations involving AC targets, the projectile–target interaction does not have spherical symmetry and the total ICSs $\sigma_R's$ must be calculated according to Equation (8).

In the case of $H^{q_H}$ and $OH^{q_{OH}}$ FF, the SLEND $P_R(\alpha, \beta, \gamma, b) = P_{H^{q_H} \text{ and } OH^{q_{OH}} \text{ FF}}(\alpha, \beta, \gamma, b)$ is the classical probability for that process and it assumes the values $P_{H^{q_H} \text{ and } OH^{q_{OH}} \text{ FF}}(\alpha, \beta, \gamma, b) = 1$, if $H^{q_H}$ and $OH^{q_{OH}}$ FF occurs and $P_{H^{q_H} \text{ and } OH^{q_{OH}} \text{ FF}}(\alpha, \beta, \gamma, b) = 0$ otherwise. The SLEND $H^{q_H}$ and $OH^{q_{OH}}$ FF total ICSs $\sigma_{H^{q_H} \text{ and } OH^{q_{OH}} \text{ FF}}$ from Equation (8) turn out to be 0.209467 Å$^2$ and 0.930301 Å$^2$ for $H^+ + (H_2O)_3$ and $H^+ + (H_2O)_4$ at $E_{Lab} = 1$ keV, respectively. The previous SLEND study of $H^+ + (H_2O)_2$ [7] reported total ICSs $\sigma_{H^{q_H} \text{ FF}}$ and $\sigma_{OH^{q_{OH}} \text{ FF}}$ of 0.5442860 Å$^2$ and 0.2753570 Å$^2$ for independent $H^{q_H}$ and $OH^{q_{OH}}$ FFs at $E_{Lab} = 1$ keV, respectively. Unfortunately, there are no alternative experimental and/or theoretical results of $H^+ + (H_2O)_{2-4}$ at $E_{Lab} = 1$ keV for comparison. It is worth noticing that in the present simulations, $H^{q_H}$ and $OH^{q_{OH}}$ FFs always occur together in a single $H^{q_H}$ and $OH^{q_{OH}}$ FF (cf. Equation (7)), while that was not the case in the previous SLEND study [7]. Taking into account that observation and the different types of ACs involved, the most that can be said when comparing the ICSs from the previous and present SLEND studies is that their values are within the same order of magnitude as one would expect.

## 4. $H^+$-induced DNA-base damage

As discussed in Section 1, cellular DNA can be damaged during PCT by collisions with primary $H^+$ projectiles and/or with secondary, tertiary, etc. $H^+$'s produced in the water radiolysis reactions. Like the bulk water involved in those reactions, the quantum-mechanics simulation of an entire DNA molecule remains unfeasible with any current quantum-mechanics method. Therefore, SLEND simulations of DNA damage reactions should be conducted on small prototypical systems such as a component or a section of a DNA molecule. As a first step towards a SLEND study of $H^+$-induced damage on DNA, we present herein the first SLEND simulations of collisions of $H^+$ projectiles with isolated DNA bases: adenine, cytosine, guanine and thymine, at $E_{Lab}$ =1.0 keV. These simulations aim at elucidating the actual damage on DNA bases attached to DNA

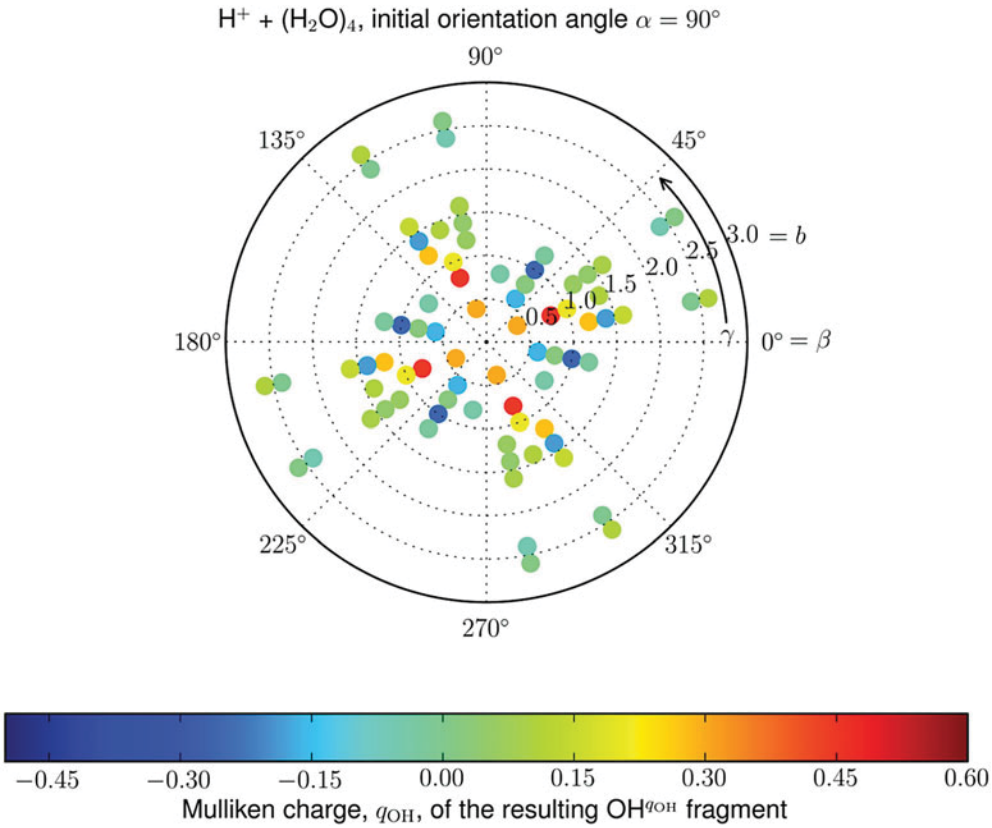


Figure 6. Occurrence and charge, $q_{OH}$, of $OH^{q_{OH}}$ in the $H^+ + (H_2O)_4$ simulation at $E_{Lab} = 1$ keV from $\alpha = 90^\circ$. Circular sectors delimit varying discrete values of $\beta$. Within each sector, $\gamma$ varies in its whole range as the polar angle from one sector's boundary to another, and the radial coordinate is the impact parameter $b$ (see text for further details).

molecules during PCT. While the chosen systems are far smaller than an entire DNA molecule, they still remain computationally demanding yet feasible for the current SLEND implementation in CSDyn. Therefore, we limit ourselves to present a preliminary exploration of the SLEND performance with $H^+ +$ DNA-base collisions. For that reason, unlike the previous $H^+ + (H_2O)_{3-4}$ investigation, a systematic study involving numerous initial projectile-target orientations and impact parameters and leading to the prediction of ICSs was not attempted with these systems. Instead, a fewer but still large number of simulations were conducted based on their potential for causing relevant PCT reactions; this allows an assessment of the SLEND's capacity of describing those reactions and an estimation of the computational cost of their subsequent systematic investigation. Consequently, only the Slater-type orbital from three primitive Gaussians (STO-3G) basis set has been employed in these exploratory studies. While we conducted several simulations with these systems, we will present below only one illustrative simulation for each tested DNA base.

The initial conditions of the present SLEND/STO-3G simulations of $H^+ +$ DNA-base collisions at $E_{Lab} = 1.0$ keV are as follows. Each DNA base is placed at rest with its centre of mass at the (0.0, 0.0, 0.0) position and with the plane (thymine) or quasi-plane (remaining bases) of their heterocyclic ring(s) placed completely (thymine) or with maximum coincidence (remaining bases) on the $xy$ plane. The $H^+$ projectile is first prepared with position $\mathbf{R}^0_{H^+}(b) = (b \geq 0, 0, -30.0)$ a.u. and momentum $\mathbf{P}^0_{H^+} = (0,\ 0,\ p^z_{H^+} > 0)$, where again $b$ is the projectile's impact parameter and $p^z_{H^+}$ corresponds to a kinetic energy $E_{Lab} = 1$ keV. The definite initial conditions of the $H^+$ projectile $\mathbf{R}^i_{H^+}$ and $\mathbf{P}^i_{H^+}$ are obtained by rotating $\mathbf{R}^0_{H^+}$ and $\mathbf{P}^0_{H^+}$ by the Euler angles $0^\circ \leq \alpha \leq 180^\circ$, $0^\circ \leq \beta < 360^\circ$ and $0^0 \leq \gamma < 360^0$ in the $y - z - z$ convention. The values of $\alpha$, $\beta$, $\gamma$ and $b$ are selected to provide trajectories that lead the $H^+$ projectile to a direct collision with selected atoms on the DNA bases. Those selected atoms will be labelled according to the standard indexes by the International Union of Pure and Applied Chemistry (IUPAC) [45] for the C atoms in the DNA-base rings. Figure 7 presents four snapshots of a SLEND/STO-3G simulation of $H^+ +$ cytosine at $E_{Lab} = 1.0$ keV where the initial $H^+$ is aimed at colliding with the C(4) atom of cytosine. In Figure 7 and in the subsequent figures about $H^+ +$ DNA-base collisions, small white, large white, red and blue spheres represent the H, C, O and N classical nuclei, respectively, while the purple clouds depict selected electron density isosurfaces.

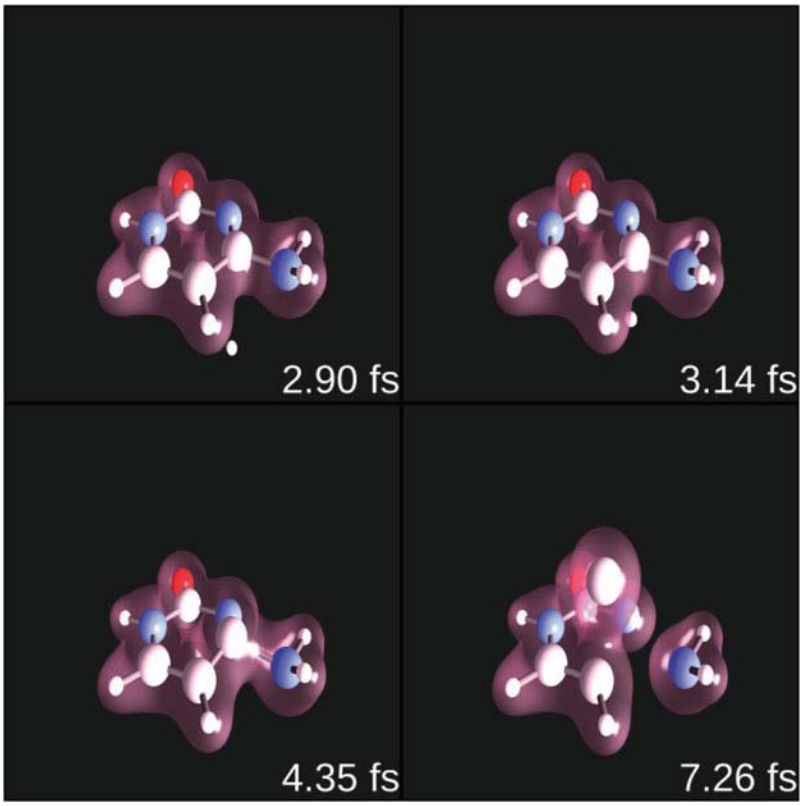


Figure 7. Proton collision with the C(4) atom of cytosine at $E_{Lab} = 1$ keV.

In Figure 7, the $H^+$ projectile collides with the C(4) atom of cytosine and scatters backward. It is obvious in Figure 7 that the collision between the $H^+$ projectile and cytosine is very violent, resulting in three fragments, namely, C [the impacted and dislodged C(4) atom], $NH_2$ and $C_3N_2OH_3$. Note that the energy transfer in this simulation is extremely localised on the impacted C(4) atom, which is violently ejected from the cytosine, while the other two fragments are less displaced and perturbed.

Figure 8 presents four snapshots of a SLEND/STO-3G simulation of $H^+ + $ thymine at $E_{Lab} = 1.0$ keV, where the initial $H^+$ is aimed at the O atom bonded to the C(4) atom of thymine. In that figure, the $H^+$ projectile strikes the selected O atom and scatters backward. The $H^+$ projectile transfers enough energy to thymine to dislodge the impacted O atom from it and leave a still bonded $C_5N_2OH_6$ fragment behind. Figure 9 presents four snapshots of a SLEND/STO-3G simulation of $H^+ + $ adenine at $E_{Lab} = 1.0$ keV, where the initial $H^+$ is aimed at colliding with one of the H atoms of the $NH_2$ group of adenine. In that figure, the $H^+$ projectile strikes the targeted H atom and scatters forward. As a result of this impact, the hit H atom is violently ejected from the $NH_2$ group while a bonded $C_5N_5H_6$ fragment is left behind. Finally, Figure 10 presents four snapshots of a SLEND/STO-3G simulation of $H^+ + $ guanine at $E_{Lab} = 1.0$ keV, where the initial $H^+$ is aimed at the C(5) atom of guanine. In that figure, the $H^+$ projectile strikes the targeted C(5) atom and scatters forward. The $H^+$ collision on the C(5) atom results in the sequential cleavage of the C(4)−C(5) (snapshot at 5.08 fs) and the C(5)−C(6) (snapshot at 6.58 fs) bonds leading to an 'open-ring' guanine. It should be further noted that the collisions in Figures 7–10 also reveal substantial base-to-proton electron-transfer processes.

The present SLEND simulations of $H^+ + $ DNA-base collisions at $E_{Lab} = 1.0$ keV reveal a wealth of chemical reactions that may be responsible for various types of $H^+$-induced damage on DNA during PCT. Based on these exploratory simulations, current SLEND research concentrates on investigating more systematically these $H^+ + $ DNA-base collisions from various initial conditions and with larger basis sets to predict dynamical properties comparable with the available experimental data. These current efforts are exemplified by our recent SLEND and SLEND/KSDFT study on the prediction of absolute ICSs for the one-electron-transfer reactions: $H^+ + B \rightarrow H + B^+$, B = adenine, cytosine, thymine and uracil, at $E_{Lab} = 80$ keV [32], in good agreement with the results from experiments [33] and from CDW and CDW-EIS theoretical studies [8].

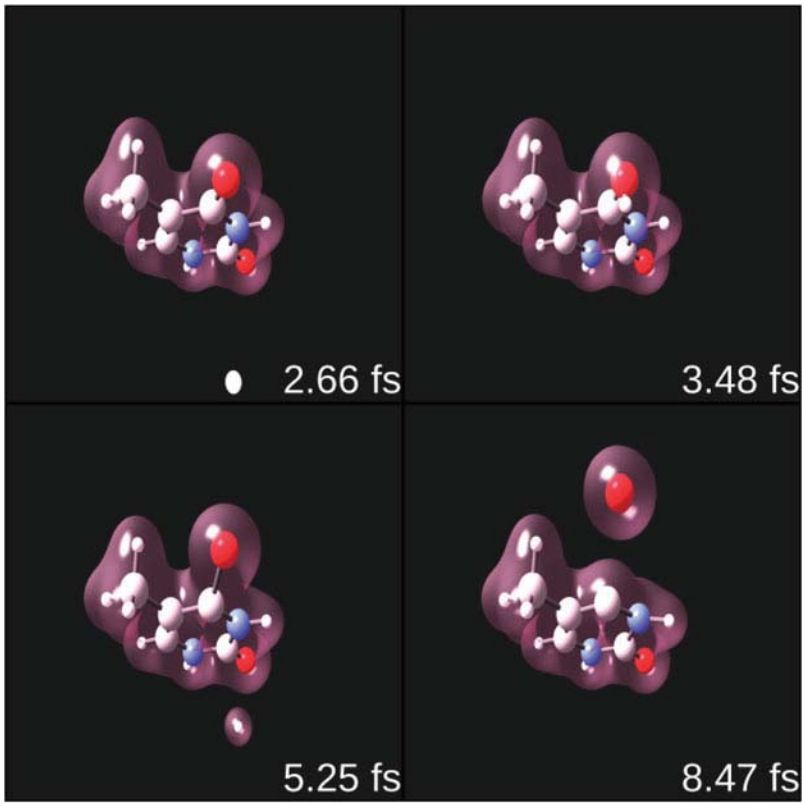


Figure 8. Proton collision with the O atom bonded to the C(4) atom of thymine at $E_{\text{Lab}} = 1.0$ keV.

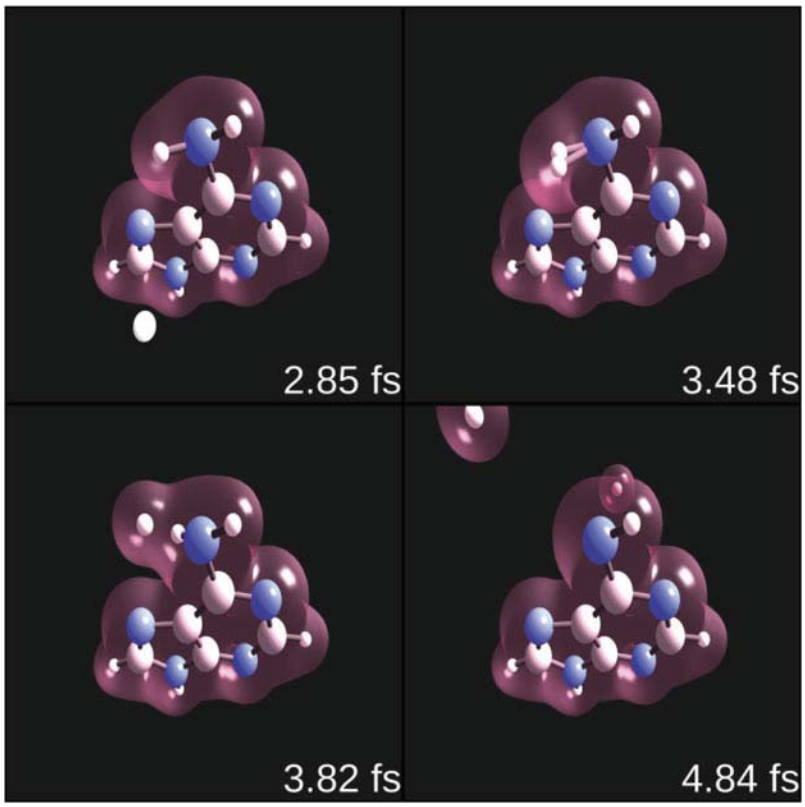


Figure 9. Proton collision with one of the H atoms of the $NH_2$ group of adenine at $E_{\text{Lab}} = 1.0$ keV.

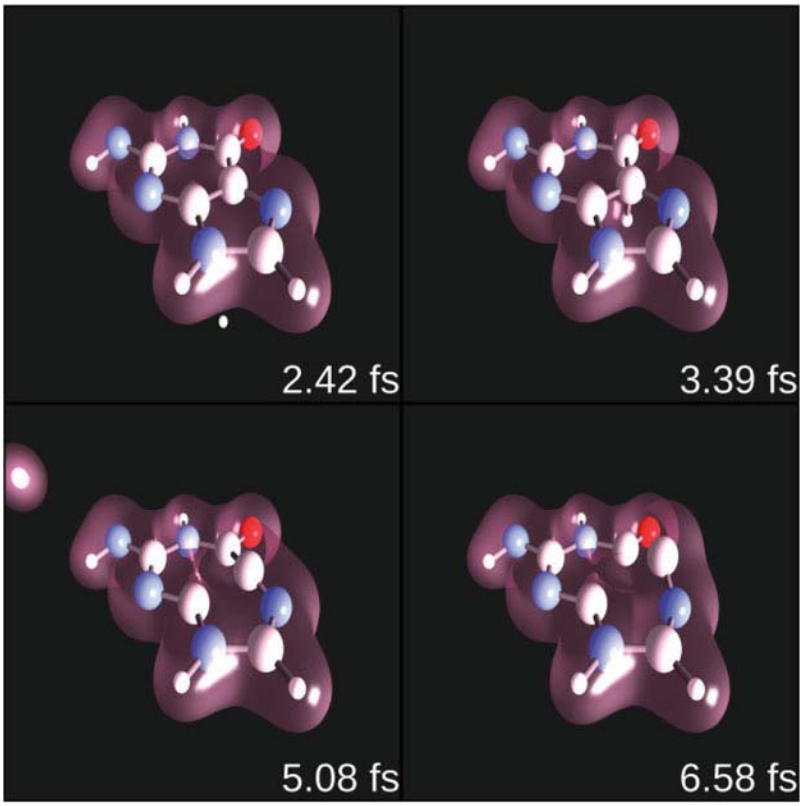


Figure 10. Proton collision with the C(5) atom of guanine at $E_{\mathrm{Lab}} = 1.0$ keV.



## 5. Conclusions

To investigate essential PCT reactions, the END method at its simplest level realisation, SLEND, [4,12,13,34] has been applied to the simulation of the $H^+ + (H_2O)_{3-4}$ and the $H^+ +$ DNA-base reactions at $E_{\mathrm{Lab}} = 1.0$ keV. These selected reactions constitute computationally feasible prototypes of bulk water radiolysis reactions and of $H^+$-induced damage on DNA during PCT, respectively. Like all END realisations, SLEND is a time-dependent, variational, non-adiabatic and direct dynamics method that treats the nuclear and electronic degrees of freedom concurrently. More specifically, SLEND utilises an electronic Thouless single-determinantal wavefunction in conjunction with a classical-mechanics description for the nuclei.

SLEND/6-31G** and SLEND + ECP/SBKJC were applied to $H^+ + (H_2O)_3$ and $H^+ + (H_2O)_4$, respectively, both at $E_{\mathrm{Lab}} = 1.0$ keV. In both systems, two main processes were predicted by SLEND: $H^+$ PS and $H^{q_H}$ and $OH^{q_{OH}}$ FF. Additionally, one case of $H_2$ and O formation was observed in $H^+ + (H_2O)_4$ from the initial orientation $\alpha - \beta - \gamma = 0^\circ - 0^\circ - 0^\circ$ and impact parameter $b = 3.6$ a.u. The two animations represented by Figures 3 and 4 illustrate cases of $H^{q_H}$ and $OH^{q_{OH}}$ FF involving the $(H_2O)_3$ and $(H_2O)_4$ ACs, respectively, while Table 2 and 3 and their pictorial polar plots in Figures 5 and 6 allow the determination of the occurrence of $H^{q_H}$ and $OH^{q_{OH}}$ FF from the reactants' initial conditions. $H^{q_H}$ and $OH^{q_{OH}}$ FF total ICSs for both reactive systems were calculated and their values were found to be consistent with comparable fragmentation ICSs calculated with SLEND for $H^+ + (H_2O)_2$ at $E_{\mathrm{Lab}} = 1.0$ keV [7]. No further comparison was possible due to the lack of additional theoretical and/or experimental results. An analysis of the Mulliken charges of the $H^{q_H}$ and $OH^{q_{OH}}$ FF products, charges that reflect the superposition of the final channel states, reveals that SLEND predicts a solvated OH· radical, $OH\cdot(H_2O)_{2-3}$, an outgoing $H^+$ projectile and an ejected H atom as the predominant and concomitant products from $H^{q_H}$ and $OH^{q_{OH}}$ FF in both reactive systems.

SLEND/STO-3G was additionally applied to $H^+$ collisions with the four DNA bases: adenine, cytosine, guanine and thymine, at $E_{\mathrm{Lab}} = 1$ keV. The aim of these exploratory simulations was to assess the SLEND's capacity of describing $H^+$-induced DNA-base damage reactions and to estimate the cost of a complete investigation of these computationally demanding systems. While several simulations of this type were conducted, we limited ourselves to present only one illustrative simulation for each tested DNA base. Animations of those simulations shown in Figures 7–10 display an astonishing wealth of vigorous damage processes induced by the $H^+$'s impact, including the removal of atoms

and groups from the DNA bases, the opening of their rings and base-to-proton electron-transfer reactions. These predicted processes may play a relevant role in the actual DNA damage during PCT. Based on these preliminary studies, a systematic SLEND investigation on these DNA-base systems is currently underway with the goal of predicting various dynamical properties to be compared with available experimental results (cf. Ref. [32]).

Present research efforts concentrate on the further investigation of the reported PCT reactions involving larger $(H_2O)_{1-6}$ ACs [43] and larger DNA components (e.g. pairs of DNA bases [4]). Such investigations are currently conducted with our new SLEND and SLEND/KSDFT code PACE (Python Accelerated Coherent-states Electron-nuclear-dynamics, T.V. Grimes and J.A. Morales, Texas Tech University, 2010-2014; cf. Ref. [4], Sect. 4). PACE incorporates various advanced computer science techniques including a mixed programming language (Python for logic flow and Fortran/C++ for calculations), intra and inter-node parallelisation, and the one-electron direct and electron-repulsion direct (OED/ERD) atomic integral package [46] from the ACES III (Advance Concept in Electronic Structure III) [47] code *inter alia*.

## Acknowledgements

The authors thank Mr. S. Hinds [Texas Tech University (TTU) chemistry undergraduate student] for his help with some $H^+ + (H_2O)_{3-4}$ simulations and Ms. A. Aguilar, Mr. B. Hernandez and Mr. Kevin Cassity (participants of the Summer Research Academy for Theoretical and Computational Chemistry in 2011, 2011 and 2012, respectively) for their help with some $H^+$ + DNA-base simulations. All the present calculations have been performed at the TTU High Performance Computer Center (TTU HPCC), the TTU Chemistry Computer Cluster (TTU CCC) and the Texas Advanced Computing Center (TACC) at the University of Texas at Austin. The authors thank TTU HPCC and TACC for providing free computer time to run some of the present calculations.

## Funding

This work is partially supported by the National Science Foundation [grant number CHE-0645374 (CAREER) and grant number CHE-0840493] (to build the TTU CCC)], and the Robert A. Welch Foundation Grant [grant number D-1539].



## References

[1] A.V. Solov'yov, E. Surdutovich, E. Scifoni, I. Mishustin, and W. Greiner, Phys. Rev. E **79**, 011909 (2009).
[2] M.A. Tabocchini, A. Campa, and V. Dini, Health Phys. **103**, 547 (2012).
[3] E. Surdutovich and A.V. Solov'yov, J. Phy. Conf. Ser. **438**, 012014 (2013).
[4] C. Stopera, T.V. Grimes, P.M. McLaurin, A. Privett, and J.A. Morales, in *Advances in Quantum Chemistry*, edited by J.R. Sabin and E.J. Brandas (Elsevier, Oxford, 2013), vol. 66, Chap. 3, p. 113.
[5] L. Pichl, M. Kimura, L. Yan, and R.J. Buenker, Trans. Nucl. Sci. **51**, 1407 (2004).
[6] R. Cabrera-Trujillo, J.R. Sabin, E. Deumens, and Y. Öhrn, in *Advances in Quantum Chemistry*, edited by J.R. Sabin and E.J. Brandas (Elsevier, Oxford, 2005), Vol. 48, p. 47.
[7] O. Quinet, E. Deumens, and Y. Öhrn, Int. J. Quant. Chem. **109**, 259 (2008).
[8] C. Champion, P.F. Weck, H. Lekadir, M.E. Galassi, O.A. Fojon, P. Abufager, R.D. Rivarola, and J. Hanssen, Phys. Med. Biol. **57**, 3039 (2012).
[9] R. Watanabe and K. Saito, Radiat. Environ. Biophys. **41**, 207 (2002).
[10] W. Friedland, P. Jacob, P. Bernhardt, H.G. Paretzke, and M. Dingfelder, Radiat. Res. **159**, 401 (2003).
[11] S. Agostinelli, J. Allison, K. Amako, J. Apostolakis, H. Araujo, P. Arce, M. Asai, D. Axen, S. Banerjee, G. Barrand, F. Behner, L. Bellagamba, J. Boudreau, L. Broglia, A. Brunengo, H. Burkhardt, S. Chauvie, J. Chuma, R. Chytracek, G. Cooperman, G. Cosmo, P. Degtyarenko, A. Dell'Acqua, G. Depaola, D. Dietrich, R. Enami, A. Feliciello, C. Ferguson, H. Fesefeldt, G. Folger, F. Foppiano, A. Forti, S. Garelli, S. Giani, R. Giannitrapani, D. Gibin, J.J. Gómez Cadenas, I. González, G. Gracia Abril, G. Greeniaus, W. Greiner, V. Grichine, A. Grossheim, S. Guatelli, P. Gumplinger, R. Hamatsu, K. Hashimoto, H. Hasui, A. Heikkinen, A. Howard, V. Ivanchenko, A. Johnson, F.W. Jones, J. Kallenbach, N. Kanaya, M. Kawabata, Y. Kawabata, M. Kawaguti, S. Kelner, P. Kent, A. Kimura, T. Kodama, R. Kokoulin, M. Kossov, H. Kurashige, E. Lamanna, T. Lampén, V. Lara, V. Lefebure, F. Lei, M. Liendl, W. Lockman, F. Longo, S. Magni, M. Maire, E. Medernach, K. Minamimoto, P. Mora de Freitas, Y. Morita, K. Murakami, M. Nagamatu, R. Nartallo, P. Nieminen, T. Nishimura, K. Ohtsubo, M. Okamura, S. O'Neale, Y. Oohata, K. Paech, J. Perl, A. Pfeiffer, M.G. Pia, F. Ranjard, A. Rybin, S. Sadilov, E. Di Salvo, G. Santin, T. Sasaki, N. Savvas, Y. Sawada, S. Scherer, S. Sei, V. Sirotenko, D. Smith, N. Starkov, H. Stoecker, J. Sulkimo, M. Takahata, S. Tanaka, E. Tcherniaev, E. Safai Tehrani, M. Tropeano, P. Truscott, H. Uno, L. Urban, P. Urban, M. Verderi, A. Walkden, W. Wander, H. Weber, J.P. Wellisch, T. Wenaus, D.C. Williams, D. Wright, T. Yamada, H. Yoshida, and D. Zschiesche, Nucl. Instrum. Methods Phys. Res. A **506**, 250 (2003).
[12] E. Deumens, A. Diz, R. Longo, and Y. Öhrn, Rev. Mod. Phys. **66**, 917 (1994).
[13] E. Deumens and Y. Öhrn, J. Phys. Chem. A **105**, 2660 (2001).
[14] E. Deumens, Y. Öhrn, and B. Weiner, J. Math. Phys. **32**, 1166 (1991).
[15] R.J. Bartlett and M. Musiał, Rev. Mod. Phys. **79**, 291 (2007).
[16] S.A. Perera, P.M. McLaurin, T.V. Grimes, and J.A. Morales, Chem. Phys. Lett. **496**, 188 (2010).
[17] L. Sun and W.L. Hase, in *Reviews in Computational Chemistry*, edited by K.B. Lipkowitz, R. Larter, and T.R. Cundari (Wiley, New York, 2003), vol. 19, p. 79.
[18] J.A. Morales, A.C. Diz, E. Deumens, and Y. Öhrn, Chem. Phys. Lett. **233**, 392 (1995).
[19] J. Morales, A. Diz, E. Deumens, and Y. Öhrn, J. Chem. Phys. **103**, 9968 (1995).
[20] D. Jacquemin, J.A. Morales, E. Deumens, and Y. Ohrn, J. Chem. Phys. **107**, 6146 (1997).
[21] M. Hedström, J.A. Morales, E. Deumens, and Y. Öhrn, Chem. Phys. Lett. **279**, 241 (1997).
[22] S.A. Malinovskaya, R. Cabrera-Trujillo, J.R. Sabin, E. Deumens, and Y. Ohrn, J. Chem. Phys. **117**, 1103 (2002).

[23] J.A. Morales, B. Maiti, Y. Yan, K. Tsereteli, J. Laraque, S. Addepalli, and C. Myers, Chem. Phys. Lett. **414**, 405 (2005).
[24] B. Maiti, R. Sadeghi, A. Austin, and J.A. Morales, Chem. Phys. **340**, 105 (2007).
[25] B. Maiti, P.M. McLaurin, R. Sadeghi, S. Ajith Perera, and J.A. Morales, Int. J. Quantum Chem. **109**, 3026 (2009).
[26] C. Stopera, B. Maiti, T.V. Grimes, P.M. McLaurin, and J.A. Morales, J. Chem. Phys. **134**, 224308 (2011).
[27] C. Stopera, B. Maiti, T.V. Grimes, P.M. McLaurin, and J.A. Morales, J. Chem. Phys. **136**, 054304 (2012).
[28] C. Stopera, B. Maiti, and J.A. Morales, Chem. Phys. Lett. **551**, 42 (2012).
[29] R. Cabrera-Trujillo, Y. Öhrn, E. Deumens, and J.R. Sabin, J. Phys. Chem. A **108**, 8935 (2004).
[30] M. Coutinho-Neto, E. Deumens, and Y. Öhrn, Int. J. Quantum Chem. **77**, 301 (2000).
[31] M. Coutinho-Neto, E. Deumens, and Y. Öhrn, J. Chem. Phys. **116**, 2794 (2002).
[32] A. Privett and J.A. Morales, Chem. Phys. Lett. **603**, 82 (2014).
[33] J. Tabet, S. Eden, S. Feil, H. Abdoul-Carime, B. Farizon, M. Farizon, S. Ouaskit, and T.D. Märk, Phys. Rev. A **82**, 022703 (2010).
[34] F. Hagelberg, *Electron Dynamics in Molecular Interactions: Principles and Applications* (World Scientific, Singapure, 2014).
[35] P. Kramer and M. Saraceno, *Geometry of the Time-Dependent Variational Principle in Quantum Mechanics* (Springer, New York, 1981).
[36] D.J. Thouless, Nucl. Phys. **21**, 225 (1960).
[37] R. Longo, A. Diz, E. Deumens, and Y. Öhrn, Chem. Phys. Lett. **220**, 305 (1994).
[38] H. Goldstein, *Classical Mechanics* (Addison-Wesley, Reading, MA, 1980).
[39] M. Krauss and W.J. Stevens, Annu. Rev. Phys. Chem. **35**, 357 (1984).
[40] P.M. McLaurin, Ph.D. thesis, Texas Tech University, 2011.
[41] S.S. Xantheas and T.H. Dunning, J. Chem. Phys. **99**, 8774 (1991).
[42] J. Morales, A. Diz, E. Deumens, and Y. Öhrn, J. Chem. Phys. **103**, 9968 (1995).
[43] A. Privett, J. Yoo, C. Stopera, and J.A. Morales, J. Chem. Phys. (2014) (unpublished).
[44] M.S. Child, *Molecular Collision Theory* (Academic Press, Inc., New York, 1974).
[45] A.D. McNaught and A. Wilkinson, *Compendium of Chemical Terminology* (Blackwell Scientific Publications, Oxford, 1997).
[46] N. Flocke and V. Lotrich, J. Comput. Chem. **29**, 2722 (2008).
[47] V. Lotrich, N. Flocke, M. Ponton, A.D. Yau, A. Perera, E. Deumens, and R.J. Bartlett, J. Chem. Phys. **128**, 194104 (2008).